Continuum Mech. Thermodyn. (2017) 29:1389–1412
DOI 10.1007/s00161-017-0589-3

ORIGINAL ARTICLE

Habib Pouriayevali · **Bai-Xiang Xu**

A study of gradient strengthening based on a finite-deformation gradient crystal-plasticity model

Received: 16 April 2017 / Accepted: 13 July 2017 / Published online: 22 July 2017

Abstract A comprehensive study on a finite-deformation gradient crystal-plasticity model which has been derived based on Gurtin's framework (Int J Plast 24:702–725, 2008) is carried out here. This systematic investigation on the different roles of governing components of the model represents the strength of this framework in the prediction of a wide range of hardening behaviors as well as rate-dependent and scale-variation responses in a single crystal. The model is represented in the reference configuration for the purpose of numerical implementation and then implemented in the FEM software ABAQUS via a user-defined subroutine (UEL). Furthermore, a function of accumulation rates of dislocations is employed and viewed as a measure of formation of short-range interactions. Our simulation results reveal that the dissipative gradient strengthening can be identified as a source of isotropic-hardening behavior, which may represent the effect of irrecoverable work introduced by Gurtin and Ohno (J Mech Phys Solids 59:320–343, 2011). Here, the variation of size dependency at different magnitude of a rate-sensitivity parameter is also discussed. Moreover, an observation of effect of a distinctive feature in the model which explains the effect of distortion of crystal lattice in the reference configuration is reported in this study for the first time. In addition, plastic flows in predefined slip systems and expansion of accumulation of GNDs are distinctly observed in varying scales and under different loading conditions.

Keywords Gradient crystal plasticity · Hardening · Finite deformation · Gradient strengthening

1 Introduction

Crystal lattices are disrupted by point, line and surface defects such as dislocations, disclinations, voids and interstitial atoms [1,2]. Experimental results have also shown that accumulation of defects gives rise to an intrinsic size-dependent response of crystalline materials along with inhomogeneous plastic flows on the micro-scale level [3–10]. Prediction of such a size-dependent response requires incorporation of atomistic slip systems, gradient description and length-scale parameters into classical plasticity models.

Pertinent works on the development of classical crystal-plasticity theory have been presented in e.g., [11–13]. The general approach is an incorporation of the Schmid law into inelastic constitute models. Concerning the size-dependence modeling, it is well accepted that extension of conventional plasticity theories to strain-gradient plasticity is a promising approach. Comprehensive reviews of strain-gradient theories have been presented in [14–17]. Studies on the non-uniform straining in crystalline materials show that flow and accumulation of dislocations play an important role in the accommodation of deformation in a crystal lattice

Communicated by Andreas Öchsner.

H. Pouriayevali (✉) · B.-X. Xu
Mechanics of Functional Materials Division, Institute of Material Science, Technische Universität Darmstadt, Jovanka-Bontschits-Strasse 2, 64287 Darmstadt, Germany
E-mail: pouriayevali@mfm.tu-darmstadt.de

[18,19]. Furthermore, it is well accepted that statistically stored dislocation (SSD) and geometrically necessary dislocation (GND) densities could be simply described by plastic flow and its gradient, respectively [3,20–22]. Geometrical foundations of dislocation density tensors associated with the torsion of crystal connection have been detailed in e.g., [1,23]. In addition to the density of line defects, a measure of density of point defects was also proposed by Naghdi and Srinivasa [24] in a finite-deformation gradient crystal-plasticity framework. Studies on relationship between dislocation densities and material shear-strength can be found in [20,21,25]. A simplest form of small-deformation higher-order strain-gradient plasticity theory was proposed by Aifantis [26], and further developed in [27,28]. Aifantis introduced the Laplacian of equivalent plastic strain into a constitutive expression. Later, a class of higher-order strain-gradient theories using a couple stress [29] work-conjugate to strain gradient was proposed in [6,30] and further generalized in [20,31,32]. It is worth mentioning that Acharya and Bassani [33,34] developed a conventional plasticity theory with an incorporation of a strain-gradient term as an internal variable in hardening modulus. This theory has standard boundary conditions and no higher-order stresses. Furthermore, a comprehensive discussion on the similarities between an extension of Cosserat framework [35,36] and strain-gradient theories has been reported by Forest et al. [37–39].

Moreover, introducing a definition of GNDs tensor into strain-gradient continuum mechanics has been of great interest [40,41], and it reveals the physical interpretation behind the concept of strain-gradient crystal-plasticity theories. Cermelli and Gurtin studied a variety of GND tensors [42,43]. Moreover, Gurtin [44] introduced a framework in development of gradient crystal-plasticity model with incorporation of a system of microscopic stresses, which is consistent with microforce balance for each independent kinematic processes [32,45–47]. This framework was greatly followed later [17,43,48–61]. Cermelli and Gurtin [43] proposed a small-deformation gradient crystal-plasticity model which employs the microforce framework and a defect energy based on the GND tensor. In this study, microscopic force is simply decomposed into distributed Peach–Koehler forces for the edge and screw dislocations [62–64]. Gurtin and Anand [55,56] modified the strain-gradient theory detailed above for an irrotational-plasticity isotropic material in the framework of small and finite deformations. A detailed study on the comparison of stain-gradient theory in small and finite deformations has been presented by Gurtin [54]. In the gradient plasticity frameworks, length-scale parameters are employed to keep the dimensional consistency [30,32]. Voyiadjis et al. investigated the identification of material length-scale parameters from micro- and nano-scale experiments [10,65,66], the resulting model is a physically based model of length-scale parameters for gradient isotropic-hardening plasticity.

As a review of recent studies on the large-deformation gradient crystal-plasticity, Clayton et al. [67] employed a three-term multiplicative decomposition of the deformation gradient and studied the distortion of crystal lattice via a framework including the concept of dislocations and disclinations. Levkovitch and Svendsen [68] proposed a reformulation of a non-local single-crystal model which is accompanied by an additional kinematic-like hardening due to GNDs. Furthermore, a crystal-plasticity model incorporating additional differential equations for the evolution of GND densities was introduced in [69,70], in this model, dissipative gradient strengthening, gradient yield strengthening and dissipative length-scale are not taken in to account. A physically based strain-gradient crystal-plasticity theory was proposed via concept of micro-stress framework in [71]. Svendsen and Bargmann [72] studied a possible extension of selected small-deformation extended crystal-plasticity models to the large-deformation ones via variational approach. Finally, Gurtin [51] introduced a finite-deformation gradient crystal-plasticity model for a single crystal. This thermodynamically consistent model is based on the system of microforce balances and derived from the principle of virtual power. The free energy comprises two parts: a hyperelastic description for large-deformation compressible material and a defect energy in a frame-invariance form based on a net dislocation density [52,73]. Moreover, a non-local rate-dependence flow rule is introduced, which incorporates an energetic back-stress, a dissipative gradient strengthening as well as dissipative self- and latent-hardening. Energetic and dissipative length-scale parameters and a function of accumulation rates of SSDs and GNDs are also taken into account.

As for numerical solution of large-deformation strain-gradient theories, an implementation method which introduces GND density as an additional nodal degree of freedom has been widely employed [69,70,74–79]. Based on this method, Bargmann et al. [80,81] studied the effect of dissipative microstress in the extension of two small-deformation yield-functions proposed in [74,82]. Kuroda also employed similar implementation method in a study of a large-strain-gradient crystal-plasticity model developed via an additional higher-order back-stress description [69,70].

It can be concluded from the literature review that an understanding of large-deformation gradient crystal-plasticity is of great interest. The model proposed by Gurtin [51] was claimed to cover a number of hardening behaviors. However, to the best of authors' knowledge, there is a lack of systematic study on the governing

components of this model, even though there are great efforts on the development of theoretical models. In the current work, the authors employ Gurtin's framework in [51] to represent a model in the reference configuration for the convenience of numerical implementation. Furthermore, a function of accumulation rates of SSDs and GNDs is employed and viewed as a measure of formation of short-range interactions which impede dislocation movements within a crystal. The model is then implemented in the FEM software ABAQUS via a user-defined subroutine (UEL). The present work reveals the capability of the model in the prediction of a wide range of hardening behaviors as well as rate-dependent and scale-variation responses in a single crystal. An observation of effect of a distinctive feature in the model which explains the effect of distortion of crystal lattice in the reference configuration, is also aimed. Moreover, plastic flows in predefined slip systems and accumulation of GNDs are distinctly observed in single crystals under different loading conditions. Effects of scale variation in expansion of directional flows and accumulation of GNDs within single crystals are also investigated and simply linked to the phenomenon 'smaller is stronger'.

In addition, Gurtin and Ohno [83] proposed a new small-deformation gradient crystal-plasticity model which incorporates an irrecoverable stored energy of cold work and represents new forms of irrecoverable microstress and irrecoverable gradient strengthening. This stored energy is a portion of plastic work done during the plastic deformation, and dominantly governed by the accumulation of GNDs [83]. It is noted that the dissipative microstress introduced in [51] plays the same role as the new form proposed in [83]. Furthermore, Gurtin emphasized that the irrecoverable stored energy may lead to isotropic hardening which is induced via the irrecoverable gradient strengthening. Motivated by these statements, an isotropic-hardening response due to the dissipative gradient strengthening is also investigated.

The present work is organized as follows. In Sect. 2, the constitutive model with respect to the reference configuration is presented. Section 3 details the two-dimensional version of the model and the implementation method. In Sect. 4, numerical results are shown, compared and discussed.

2 Formulation

In this section, a finite-deformation gradient crystal-plasticity framework which has been proposed by Gurtin [51] in the deformed configuration is employed to represent a model with respect to the reference configuration in order to facilitate the numerical implementation and development of a user-defined subroutine (UEL) in the finite-element software ABAQUS.

2.1 Kinematics in a single crystal

We begin with

$$\mathbf{F} = \mathbf{F}^{\mathrm{e}}\mathbf{F}^{\mathrm{p}}, \quad \mathbf{C}^{\mathrm{e}} = \mathbf{F}^{\mathrm{e}\mathrm{T}}\mathbf{F}^{\mathrm{e}}, \quad \mathbf{E}^{\mathrm{e}} = \frac{1}{2}\left(\mathbf{C}^{\mathrm{e}} - \mathbf{I}\right) \quad \text{and} \quad \mathbf{L} = \mathbf{L}^{\mathrm{e}} + \mathbf{F}^{\mathrm{e}}\mathbf{L}^{\mathrm{p}}\mathbf{F}^{\mathrm{e}^{-1}}, \tag{1}$$

where $\mathbf{F}$ represents the deformation gradient tensor, $\mathbf{F}^{\mathrm{e}}$ denotes the elastic distortion, $\mathbf{F}^{\mathrm{p}}$ represents an inelastic deformation, where $\det \mathbf{F}^{\mathrm{p}} = 1$. $\mathbf{C}^{\mathrm{e}}$ is the right Cauchy-Green elastic tensor, $\mathbf{E}^{\mathrm{e}}$ is the Green-Lagrangian elastic strain tensor, and $\mathbf{I}$ is the identity tensor. $\mathbf{L}^{\mathrm{e}}$ and $\mathbf{L}^{\mathrm{p}}$ represent the elastic and plastic distortion-rate tensors, and $\mathbf{L}^{\mathrm{p}}$ is expressed as

$$\mathbf{L}^{\mathrm{p}} = \sum\nolimits_{\alpha} \upsilon^{\alpha}\mathbb{S}^{\alpha}, \tag{2}$$

where α is a slip-system number, υ^{α} is a flow-rate scalar, and $\mathbb{S}^{\alpha}$ is the Schmid tensor which is defined by

$$\mathbb{S}^{\alpha} = \mathbf{s}^{\alpha} \otimes \mathbf{m}^{\alpha} \quad \text{and} \quad \mathbf{l}^{\alpha} = \mathbf{m}^{\alpha} \times \mathbf{s}^{\alpha}. \tag{3}$$

Here, $\mathbf{s}^{\alpha}$, $\mathbf{m}^{\alpha}$ and $\mathbf{l}^{\alpha}$ are, respectively, the slip direction, the normal vector of slip plane and the glide direction of the screw dislocations (Sect. 2.2) which are constant vectors in the intermediate space [84] and vary in the reference configurations [54] as

$$\mathbf{s}_r^{\alpha} = \mathbf{F}^{\mathrm{p}^{-1}}\mathbf{s}^{\alpha}, \quad \mathbf{m}_r^{\alpha} = \mathbf{F}^{\mathrm{p}^{\mathrm{T}}}\mathbf{m}^{\alpha} \quad \text{and} \quad \mathbf{l}_r^{\alpha} = \mathbf{F}^{\mathrm{p}^{-1}}\mathbf{l}^{\alpha}. \tag{4}$$

In this study, r stands for the reference configuration. As an explanation of the vector mapping in Eq. (4), Gurtin et al. stated that "Some readers may disagree with this: In the literature one sometimes finds the assertion,

either verbally or implicitly via a figure, that the undistorted lattice resides in the reference space (and is hence material). We believe this to be a misconception. Physically, because a flow of dislocations involves a flow of material relative to the undistorted lattice, lattice vectors cannot be material" (Section 91.2 in [47]).

2.2 Power expenditures, force balances and dislocation densities

Consider an arbitrary subregion P of the reference body, the internal and external power expenditures $\mathcal{W}_{\text{int}}$ and $\mathcal{W}_{\text{ext}}$ are expressed in the reference configuration by

$$\mathcal{W}_{\text{int}}(P) = \int_P \mathbf{P}^{\text{e}} : \dot{\mathbf{F}}^{\text{e}} \mathrm{d}V + \sum_\alpha \int_p (\pi^\alpha \upsilon^\alpha + \boldsymbol{\xi}^\alpha \cdot \nabla \upsilon^\alpha) \mathrm{d}V, \tag{5}$$

$$\mathcal{W}_{\text{ext}}(P) = \int_P \mathbf{b} \cdot \boldsymbol{v} \mathrm{d}V + \int_{\partial P} \mathbf{p}\,(\mathbf{n}) \cdot \boldsymbol{v} \mathrm{d}A + \sum_\alpha \int_{\partial P} \boldsymbol{\xi}\,(\mathbf{n})^\alpha\, \upsilon^\alpha \mathrm{d}A, \tag{6}$$

where $\mathbf{P}^{\text{e}}$ represents the first Piola elastic-stress tensors, π^α is a scalar microforce per unit reference volume and $\boldsymbol{\xi}^\alpha$ is a microstress vector, expends power over $\nabla \upsilon^\alpha$ per unit reference volume. $\mathbf{b}$ is a macroscopic body force per unit reference volume, $\mathbf{p}\,(\mathbf{n})$ is a macroscopic surface traction, $\boldsymbol{v}$ is a velocity vector, $\mathbf{n}$ is an outward unit vector on the boundary in the reference configuration, and $\boldsymbol{\xi}\,(\mathbf{n})^\alpha$ is a scalar microtraction. ∇ denotes the gradient operation in the reference configuration. In addition, employing the principle of virtual power [49] yields the macroscopic and microscopic force balances as well as the macroscopic and microscopic traction conditions as follows:

$$\text{Div}\,\mathbf{P} + \mathbf{b} = \mathbf{0}, \quad \tau^\alpha - \pi^\alpha + \text{Div}\,\boldsymbol{\xi}^\alpha = 0, \tag{7}$$

$$\mathbf{p}\,(\mathbf{n}) = \mathbf{P}\mathbf{n} \quad \text{and} \quad \boldsymbol{\xi}\,(\mathbf{n})^\alpha = \boldsymbol{\xi}^\alpha \cdot \mathbf{n}. \tag{8}$$

Here, Div denotes the divergence operation in the reference configuration, $\mathbf{P} = \mathbf{P}^{\text{e}}\mathbf{F}^{\text{p}^{-\text{T}}}$ represents the first Piola–Kirchhoff stress and $\tau^\alpha = \mathbf{C}^{\text{e}}\mathbf{S}^{\text{e}} : \mathbb{S}^\alpha$ is the resolved shear stress, where $\mathbf{S}^{\text{e}}$ represents the second Piola elastic-stress. In the finite-deformation crystal plasticity description [51,54],

$$\dot{\rho}^\alpha_{\vdash} = -\mathbf{s}^\alpha_r \cdot \nabla \upsilon^\alpha \quad \text{and} \quad \dot{\rho}^\alpha_{\odot} = \mathbf{l}^\alpha_r \cdot \nabla \upsilon^\alpha \tag{9}$$

are directional derivatives of the slip rate in the glide directions $-\mathbf{s}^\alpha_r$ and $\mathbf{l}^\alpha_r$, $\rho^\alpha_{\vdash}$ and $\rho^\alpha_{\odot}$ denote the edge and screw dislocation densities.[1]

2.3 Free-energy imbalance

Guided by the second law of thermodynamics and the balanced power [49], the local dissipation inequality may be rewritten as

$$\dot{\Psi} - \mathbf{S}^{\text{e}} : \dot{\mathbf{E}}^{\text{e}} - \sum_\alpha \left(\pi^\alpha \upsilon^\alpha + \boldsymbol{\xi}^\alpha \cdot \nabla \upsilon^\alpha\right) \leq 0, \tag{10}$$

where $\Psi = \Psi^{\text{e}} + \Psi^{\rho}$ denotes a stored free energy per unit reference volume and comprises an elastic strain-energy Ψ^{e} and a defect energy Ψ^{ρ}. Ψ^{e} is given in a form of compressible Neo-Hookean energy density by

$$\Psi^{\text{e}} = \frac{\mu}{2}\left(\text{I}_1 - 3 - \ln \text{I}_3\right) + \frac{\lambda}{2}\left(\ln \text{I}_3^{1/2}\right)^2, \tag{11}$$

where I_1 and I_3 are the first and third invariants of $\mathbf{C}^{\text{e}}$, μ the shear modulus and λ the Lame parameter [85]. A quadratic defect energy Ψ^{ρ} and its rate form are also given by

[1] $\rho^\alpha_{\vdash}$ and $\rho^\alpha_{\odot}$ are in units of length^{-1}, and are signed. To emphasize a difference in notation, each continuum-mechanical density ρ^α can be converted to a materials-science density ϱ^α via the transformation $\rho^\alpha = b\varrho^\alpha$, b is the magnitude of material Burgers vector [48].

$$\Psi^{\rho} = \frac{1}{2} S_0 L_1^2 \sum_{\alpha} \left(\left| \rho_{\vdash}^{\alpha} \right|^2 + \left| \rho_{\odot}^{\alpha} \right|^2 \right),$$
$$\dot{\Psi}^{\rho} = S_0 L_1^2 \sum_{\alpha} \left(-\rho_{\vdash}^{\alpha} \mathbf{s}_r^{\alpha} + \rho_{\odot}^{\alpha} \mathbf{l}_r^{\alpha} \right) \cdot \nabla \upsilon^{\alpha} \tag{12}$$

where S_0 is a slip resistance and L_1 is an energetic length-scale parameter. It is worth mentioning that other forms of energetic defect energy such as rank-one, logarithmic and power-law have been employed in recent studies [73,86–90], and numerical results based on the models in [87,89,90] show that a jump in energetic cyclic stress–strain response is observed at the area of change of sign of plastic flow. Such a behavior is not observed via the quadratic form of energetic defect energy which is employed in this study [Sect. 4.2, Case study (1)].

2.4 Constitutive model

By considering the free energy Ψ, the local dissipation inequality in Eq. (10) is rewritten as

$$\left(\frac{\partial \Psi^{\mathrm{e}}}{\partial \mathbf{E}^{\mathrm{e}}} - \mathbf{S}^{\mathrm{e}} \right) : \dot{\mathbf{E}}^{\mathrm{e}} + S_0 L_1^2 \sum_{\alpha} \left(-\rho_{\vdash}^{\alpha} \mathbf{s}_r^{\alpha} + \rho_{\odot}^{\alpha} \mathbf{l}_r^{\alpha} \right) \cdot \nabla \upsilon^{\alpha} - \sum_{\alpha} \left(\pi^{\alpha} \upsilon^{\alpha} + \boldsymbol{\xi}^{\alpha} \cdot \nabla \upsilon^{\alpha} \right) \leq 0 \tag{13}$$

The energetic and dissipative microstresses are defined via $\boldsymbol{\xi}^{\alpha} = \boldsymbol{\xi}_{\mathrm{eng}}^{\alpha} + \boldsymbol{\xi}_{\mathrm{dis}}^{\alpha}$; thus, a reduced inequality is derived in

$$\frac{\partial \Psi^{\mathrm{e}}}{\partial \mathbf{E}^{\mathrm{e}}} = \mathbf{S}^{\mathrm{e}}, \quad \boldsymbol{\xi}_{\mathrm{eng}}^{\alpha} = S_0 L_1^2 \left(-\rho_{\vdash}^{\alpha} \mathbf{s}_r^{\alpha} + \rho_{\odot}^{\alpha} \mathbf{l}_r^{\alpha} \right), \quad \sum_{\alpha} \left(\pi^{\alpha} \upsilon^{\alpha} + \boldsymbol{\xi}_{\mathrm{dis}}^{\alpha} \cdot \nabla \upsilon^{\alpha} \right) \geq 0. \tag{14}$$

Equation $(14)_2$ shows that the energetic microstress $\boldsymbol{\xi}_{\mathrm{eng}}^{\alpha}$ is an in-slip-plane vector. Consequently, $\boldsymbol{\xi}_{\mathrm{dis}}^{\alpha}$ is assumed to be tangential to the slip plane and the reduced inequality in Eq. $(14)_3$ is redefined in

$$\sum_{\alpha} \left(\pi^{\alpha} \upsilon^{\alpha} + \boldsymbol{\xi}_{\mathrm{dis}}^{\alpha} \cdot \nabla^{\alpha} \upsilon^{\alpha} \right) \geq 0, \tag{15}$$

where $\nabla^{\alpha} \upsilon^{\alpha} = \bar{\mathbb{P}} \nabla \upsilon^{\alpha} = \nabla \upsilon^{\alpha} - \left(\bar{\mathbf{m}}_r^{\alpha} \cdot \nabla \upsilon^{\alpha} \right) \bar{\mathbf{m}}_r^{\alpha}$, $\bar{\mathbb{P}} = \mathbf{I} - \bar{\mathbf{m}}_r^{\alpha} \otimes \bar{\mathbf{m}}_r^{\alpha}$ and $\bar{\mathbf{m}}_r^{\alpha} = \frac{\mathbf{m}_r^{\alpha}}{|\mathbf{m}_r^{\alpha}|}$.

2.4.1 Constitutive relations for π^{α} and ξ_{dis}^{α}

To ensure Eq. (15), a strong formulation of the reduced inequality is assumed as

$$\pi^{\alpha} \upsilon^{\alpha} \geq 0 \quad \text{and} \quad \boldsymbol{\xi}_{\mathrm{dis}}^{\alpha} \cdot \nabla^{\alpha} \upsilon^{\alpha} \geq 0, \tag{16}$$

and conventional power-law model is employed to define π^{α} and $\boldsymbol{\xi}_{\mathrm{dis}}^{\alpha}$ [2] in

$$\pi^{\alpha} = S^{\alpha} \left(\frac{\upsilon^{\alpha}}{\upsilon_0} \right)^m \frac{\upsilon^{\alpha}}{|\upsilon^{\alpha}|}, \quad \pi^{\alpha} \upsilon^{\alpha} = S^{\alpha} \left(\frac{\upsilon^{\alpha}}{\upsilon_0} \right)^m |\upsilon^{\alpha}| \geq 0,$$
$$\boldsymbol{\xi}_{\mathrm{dis}}^{\alpha} = L_2^2 S^{\alpha} \left(\frac{d^{\alpha}}{d_0} \right)^q \frac{\nabla^{\alpha} \upsilon^{\alpha}}{d^{\alpha}}, \quad \boldsymbol{\xi}_{\mathrm{dis}}^{\alpha} . \nabla^{\alpha} \upsilon^{\alpha} = L_2^2 S^{\alpha} \left(\frac{d^{\alpha}}{d_0} \right)^q \frac{|\nabla^{\alpha} \upsilon^{\alpha}|^2}{d^{\alpha}} \geq 0,$$
$$d^{\alpha} = L_2 \left| \nabla^{\alpha} \upsilon^{\alpha} \right|, \quad \dot{S}^{\alpha} = \sum_{\beta} \mathrm{H}^{\alpha\beta} \phi^{\beta}, \; S^{\alpha}(x, 0) = S_y,$$
$$\mathrm{H}^{\alpha\beta} = \left[\varkappa_{\alpha\beta} h(S^{\beta}) \right], \quad \phi^{\beta} = \sqrt{{\upsilon_{\mathrm{acc}}^{\beta}}^2 + L_2^2 {\dot{\rho}_{\mathrm{acc}}^{\beta}}^2}. \tag{17}$$

Here, q and m are rate-sensitivity parameters, υ_0 and d_0 are constant positive-valued reference flow rates, L_2 is a dissipative length-scale parameter, S^{α} is a positive-valued slip resistance, ϕ^{β} is a measure of accumulation

[2] By considering the strong formulation of inequality, uncoupled forms of power laws in π^{α} and $\boldsymbol{\xi}_{\mathrm{dis}}^{\alpha}$ are defined, it is similar to the formulation in Lele and Anand [49] and in the spirit of formulation in Gurtin [51].

rate of dislocations, S_y is an initial coarse-grain shear resistance, $\mathrm{H}^{\alpha\beta}$ is a stiffness matrix, $h(S^\beta)$ is a self-hardening function and $\varkappa_{\alpha\beta}$ is an interaction constant. $\varkappa_{\alpha\beta} = 1$ if $\mathbf{m}^\alpha = \pm\mathbf{m}^\beta$ and $\varkappa_{\alpha\beta} = \kappa$ otherwise, κ represents a ratio of latent-hardening rate to self-hardening rate. In this study, ϕ^β is defined as an accumulation rate of dislocations and represents a measure of formation of short-range interactions between all dislocations, i.e., both SSDs and GNDs. These interactions impede the dislocation movements and render a dissipative hardening [78]. $\upsilon^\alpha_{\mathrm{acc}}$ and $\dot{\rho}^\alpha_{\mathrm{acc}}$ represent the accumulation rate of SSDs and GNDs, respectively [48,82,89,91],

$$\upsilon^\beta_{\mathrm{acc}} = \left|\upsilon^\beta\right| \quad \text{and} \quad \dot{\rho}^\beta_{acc} = \sqrt{\left|\dot{\rho}^\beta_{\vdash}\right|^2 + \left|\dot{\rho}^\beta_{\odot}\right|^2}. \tag{18}$$

2.4.2 Flow rule

The microscopic force balance Eq. $(7)_2$ takes the following form via $\boldsymbol{\xi}^\alpha = \boldsymbol{\xi}^\alpha_{\mathrm{eng}} + \boldsymbol{\xi}^\alpha_{\mathrm{dis}}$,

$$\tau^\alpha + \mathrm{Div}\boldsymbol{\xi}^\alpha_{\mathrm{eng}} = \pi^\alpha - \mathrm{Div}\boldsymbol{\xi}^\alpha_{\mathrm{dis}}. \tag{19}$$

Substitution of Eqs. $(14)_2$ and (17) into Eq. (19) results in

$$\tau^\alpha + \underbrace{S_0 L_1^2 \mathrm{Div}\left(-\rho^\alpha_{\vdash}\mathbf{s}^\alpha_r + \rho^\alpha_{\odot}\mathbf{l}^\alpha_r\right)}_{\text{(I)}} = \underbrace{S^\alpha\left(\frac{\upsilon^\alpha}{\upsilon_0}\right)^m \frac{\upsilon^\alpha}{|\upsilon^\alpha|}}_{\text{(II)}} - \underbrace{\mathrm{Div}\left(L_2^2 S^\alpha\left(\frac{d^\alpha}{d_0}\right)^q \frac{\nabla^\alpha\upsilon^\alpha}{d^\alpha}\right)}_{\text{(III)}}. \tag{20}$$

The flow rule in Eq. (20) is governed by three different components. The term (I) represents an energetic hardening defined via the defect energy and is independent of υ^α sign. Therefore, term (I) is expected to show back-stress effect and the Bauschinger-like phenomenon. The terms (II) and (III) express dissipative hardening and strengthening via a dissipative microforce, power-conjugate to υ^α, and a dissipative microstress power-conjugate to $\nabla^\alpha\upsilon^\alpha$, respectively. Similar to many other gradient theories, the length-scale parameters L_1 and L_2 are ad hoc parameters [47] and keep the dimensional consistency [30,32]. However, a built-in gradient length-scale $\frac{\mu b}{\bar{S}}$ in a small-deformation theory based on a GND self-energy near the grain boundaries was proposed in [73,89], where μ is the shear modulus, b is the magnitude of material Burgers vector, and $\bar{S}$ is the initial slip resistance (Section 8 in [48]). This small-deformation theory showed good agreements with a series of experiments from submicron to several microns range of grain sizes [73,89] and yielded an observation of size dependency of the initial slip resistance which reveals the physical interpretation behind the concept of length-scale parameters.

2.5 Microscopic boundary conditions

Considering a higher-order strain-gradient theory requires concomitantly a microscopic boundary condition and results in an expenditure of microscopic power $\int_{\partial P}\boldsymbol{\xi}(\mathbf{n})^\alpha\upsilon^\alpha dA$ defined in Eq. (6). In this study, a microscopic boundary with a null power-expenditure is defined by

$$\boldsymbol{\xi}(\mathbf{n})^\alpha\,\upsilon^\alpha = (\boldsymbol{\xi}^\alpha\cdot\mathbf{n})\,\upsilon^\alpha = 0, \tag{21}$$

and it is simply satisfied via considering two idealized boundary conditions—microscopically free boundary through $\boldsymbol{\xi}^\alpha\cdot\mathbf{n} = 0$, and microscopically hard boundary via $\upsilon^\alpha = 0$. A more comprehensive study on the powerless boundaries could be found in [92].

3 Two-dimensional version of the model and implementation method

A two-dimensional version of the model is introduced here. $\nabla\upsilon^\alpha$, $\mathbf{m}^\alpha$ and $\mathbf{s}^\alpha$ are in-plane vectors, and $\mathbf{e} = \mathbf{m}^\alpha\times\mathbf{s}^\alpha$ is an out-of-plane vector. The rates of dislocation densities are given by

$$\dot{\rho}^\alpha_{\vdash} = -\mathbf{s}^\alpha_r\cdot\nabla\upsilon^\alpha \quad \text{and} \quad \dot{\rho}^\alpha_{\odot} = \mathbf{e}\cdot\nabla\upsilon^\alpha = 0 \tag{22}$$

where $\rho^{\alpha}_{\vdash}(x,0) = \rho^{\alpha}_{\odot}(x,0) = 0$. Then, the flow rule in Eq. (20) is rewritten as

$$\tau^{\alpha} + \underbrace{S_0 L_1^2 \mathrm{Div}\left(-\rho^{\alpha}_{\vdash}\mathbf{s}^{\alpha}_{r}\right)}_{\text{(I)}} = \underbrace{S^{\alpha}\left(\frac{\upsilon^{\alpha}}{\upsilon_0}\right)^{m}\frac{\upsilon^{\alpha}}{|\upsilon^{\alpha}|}}_{\text{(II)}} - \underbrace{\mathrm{Div}\left(L_2^2 S^{\alpha}\left(\frac{d^{\alpha}}{d_0}\right)^{q}\frac{\nabla^{\alpha}\upsilon^{\alpha}}{d^{\alpha}}\right)}_{\text{(III)}}, \tag{23}$$

where

$$\nabla^{\alpha}\upsilon^{\alpha} = \left(\mathbf{s}^{\alpha}_{r}\cdot\nabla\upsilon^{\alpha}\right)\mathbf{s}^{\alpha}_{r}/\left|\mathbf{s}^{\alpha}_{r}\right|^2, \quad d^{\alpha} = L_2\left|\nabla^{\alpha}\upsilon^{\alpha}\right|, \quad \dot{S}^{\alpha} = \sum_{\beta}\mathrm{H}^{\alpha\beta}\phi^{\beta},\ S^{\alpha}(x,0) = S_y. \tag{24}$$

Due to the limited information on q and for the sake of simplicity, $q = 1$ and $\nabla S^{\alpha} = \mathbf{0}$ in term (III) are assumed in the numerical simulations. In this way, Eq. (23) is reduced to

$$\tau^{\alpha} + \underbrace{S_0 L_1^2 \mathrm{Div}\left(-\rho^{\alpha}_{\vdash}\mathbf{s}^{\alpha}_{r}\right)}_{\text{(I)}} = \underbrace{S^{\alpha}\left(\frac{\upsilon^{\alpha}}{\upsilon_0}\right)^{m}\frac{\upsilon^{\alpha}}{|\upsilon^{\alpha}|}}_{\text{(II)}} - \underbrace{S^{\alpha}L_2^2\frac{\mathrm{Div}\,\nabla^{\alpha}\upsilon^{\alpha}}{d_0}}_{\text{(III)}}. \tag{25}$$

The two-dimensional version of the model is implemented via a user-defined subroutine (UEL) in the finite-element software ABAQUS. An implementation method introducing the rate of dislocation density $\dot{\rho}^{\alpha}_{\vdash} = -\mathbf{s}^{\alpha}_{r}\cdot\nabla\upsilon^{\alpha}$ as an additional nodal degree of freedom, is employed. A plane-strain quadratic-element (8-node element with 9 integration points) is defined, and the flow rule Eq. (25) is solved at the integration points to obtain the plastic flow in each slip system via the Newton–Raphson scheme. This implementation method has been widely used by others [69–71,74,76,78,81].

3.1 Calculation within an element

The nodal degrees of freedom: the displacement components u_1, u_2 and $\dot{\rho}^{\alpha}_{\vdash}$, are given by the finite-element software. At a time-step $\Delta t = t_{n+1} - t_n$, $\rho^{\alpha}_{\vdash n+1} = \Delta t\,\dot{\rho}^{\alpha}_{\vdash} + \rho^{\alpha}_{\vdash n}$ is updated, and the deformation gradient $\mathbf{F}_{n+1}$,

$$\begin{aligned}
&\mathrm{Div}\left(-\rho^{\alpha}_{\vdash n+1}\mathbf{s}^{\alpha}_{r}\right) = -\nabla\rho^{\alpha}_{\vdash n+1}\cdot\mathbf{s}^{\alpha}_{r} - \rho^{\alpha}_{\vdash n+1}\,\mathrm{Div}\,\mathbf{s}^{\alpha}_{r} \quad \text{and}\\
&\mathrm{Div}\,\nabla^{\alpha}\upsilon^{\alpha} = \mathrm{Div}\left(-\dot{\rho}^{\alpha}_{\vdash}\mathbf{s}^{\alpha}_{r}/\left|\mathbf{s}^{\alpha}_{r}\right|^2\right) = -\nabla\dot{\rho}^{\alpha}_{\vdash}\cdot\mathbf{s}^{\alpha}_{r}/\left|\mathbf{s}^{\alpha}_{r}\right|^2 - \dot{\rho}^{\alpha}_{\vdash}\,\mathrm{Div}\left(\mathbf{s}^{\alpha}_{r}/\left|\mathbf{s}^{\alpha}_{r}\right|^2\right)
\end{aligned} \tag{26}$$

are computed at the integration points.[3] The quantity $\mathbf{F}^{\mathrm{p}}_{n}$ which has been already saved in the last time-step is employed, and trial quantities

$$\begin{aligned}
&\mathbf{F}^{\mathrm{e}}_{n+1}{}^{\mathrm{trial}} = \mathbf{F}_{n+1}\mathbf{F}^{\mathrm{p}^{-1}}_{n},\\
&\mathbf{C}^{\mathrm{e}}_{n+1}{}^{\mathrm{trial}} = \mathbf{F}^{\mathrm{e}\,\mathrm{T}}_{n+1}{}^{\mathrm{trial}}\mathbf{F}^{\mathrm{e}}_{n+1}{}^{\mathrm{trial}} \quad \text{and}\\
&\tau^{\alpha}_{n+1}{}^{\mathrm{trial}} = \mathbf{C}^{\mathrm{e}}_{n+1}{}^{\mathrm{trial}}\mathbf{S}^{\mathrm{e}}_{n+1}{}^{\mathrm{trial}} : \mathbb{S}^{\alpha}
\end{aligned} \tag{27}$$

are calculated. The flow rule Eq. (25) is solved at the integration points and the flow rate υ^{α}_{n+1} is obtained via the Newton–Raphson scheme, $\mathbf{F}^{\mathrm{p}}_{n+1}$ may be updated via a semi-implicit Euler method[4] in the form

$$\mathbf{F}^{\mathrm{p}}_{n+1} = \boldsymbol{\Gamma}\left(\Delta t\sum_{\alpha}\upsilon^{\alpha}_{n+1}\mathbb{S}^{\alpha} + \mathbf{I}\right)\mathbf{F}^{\mathrm{p}}_{n}, \tag{28}$$

where $\boldsymbol{\Gamma}(\mathbf{A}) = (\det\mathbf{A})^{-\frac{1}{3}}\mathbf{A}$ enforces $\det\mathbf{F}^{\mathrm{p}} = 1$. Finally, $\mathbf{F}^{\mathrm{p}}_{n+1}$ is saved for a new calculation in the next time-step, and $\mathbf{F}^{\mathrm{e}}_{n+1}$ and $\mathbf{C}^{\mathrm{e}}_{n+1}$ are calculated and employed in the derivation of elemental stiffness matrix and elemental residual which are detailed in the following section.

[3] Effect of distortion of crystal lattice in the reference configuration ($\mathrm{Div}\,\mathbf{s}^{a}_{r}$) is discussed in Sect. 4.4.

[4] The form of $\mathbf{F}^{\mathrm{p}}_{n+1} - \mathbf{F}^{\mathrm{p}}_{n} = \left(\Delta t\sum_{\alpha}\upsilon^{\alpha}_{n+1}\mathbb{S}^{\alpha}\right)\mathbf{F}^{\mathrm{p}}_{n+1}$ renders a fully implicit method.

3.2 Weak forms and elemental residual

Here, weak forms of the macroscopic force balance and the rate of dislocation density $\dot{\rho}^{\alpha}_{\vdash}$ are detailed. The macroscopic force balance via a vectorial set of virtual velocity descriptor $\boldsymbol{\varphi}$ is redefined in

$$\int_P (\mathbf{P} : \nabla\boldsymbol{\varphi})\, \mathrm{d}V - \int_P \mathbf{b}\cdot\boldsymbol{\varphi}\mathrm{d}V - \int_{\partial P} \mathbf{p}\,(\mathbf{n})\cdot\boldsymbol{\varphi}\mathrm{d}A = 0. \tag{29}$$

Following the variational approach leading to the finite-element discretization technique (Section 8 in [93]), a virtual displacement field $\boldsymbol{\varphi} = \delta\boldsymbol{u}$ is introduced. In the absence of the body force and considering a null external-work due to the boundary conditions, the variational equation is given by

$$\delta\Pi = \delta W_{\mathrm{int}} - \delta W_{\mathrm{ext}} = \sum_{j}^{\text{elements}} \sum_{i}^{\text{nodes}} \delta\boldsymbol{u}_i^{e\mathrm{T}} \int_{\Omega_j} \left(\mathbf{B}_i^{\mathrm{T}} : \mathbf{S}\right) \mathrm{d}V, \tag{30}$$

where j and i stand for the element and node numbers, $\delta\boldsymbol{u}_i^e$ represents a virtual displacement vector. $\mathbf{B}_i = \boldsymbol{\mathcal{D}}_r\mathbf{N}_i$, where $\boldsymbol{\mathcal{D}}_r$ is a nonlinear differential operating matrix with respect to the reference configuration, $\mathbf{N}_i$ is an elemental shape function (Section 5 in [94]), and $\mathbf{S}$ is the second Piola–Kirchhoff stress. Therefore, the elemental residual is defined in the form

$$R^e_{\boldsymbol{u}} = \sum_{i}^{\text{nodes}} R^{ei}_{\boldsymbol{u}} = \sum_{i}^{\text{nodes}} \int \left(\mathbf{B}_i^{\mathrm{T}} : \mathbf{S}\right) \mathrm{d}V. \tag{31}$$

Furthermore, the rate of dislocation density $\dot{\rho}^{\alpha}_{\vdash} = -\mathbf{s}^{\alpha}_r \cdot \nabla\upsilon^{\alpha}$ is formulated in a weak form by

$$\int_P \dot{\rho}^{\alpha}_{\vdash}\delta\dot{\rho}^{\alpha}_{\vdash}\, \mathrm{d}V \; - \int_P \nabla\cdot\left(\delta\dot{\rho}^{\alpha}_{\vdash}\mathbf{s}^{\alpha}_r\right)\upsilon^{\alpha}\, \mathrm{d}V \; + \int_{\partial P} \upsilon^{\alpha}\left(\delta\dot{\rho}^{\alpha}_{\vdash}\mathbf{s}^{\alpha}_r\right)\cdot\mathbf{n}_{\partial P}\, \mathrm{d}A \; = 0. \tag{32}$$

By considering the microscopically hard boundary condition $\upsilon^{\alpha} = 0$ introduced in Sect. 2.5, Eq. (32) may be rewritten in

$$\int_P \dot{\rho}^{\alpha}_{\vdash}\delta\dot{\rho}^{\alpha}_{\vdash}\, \mathrm{d}V \; - \int_P \left(\mathbf{s}^{\alpha}_r \cdot \nabla\delta\dot{\rho}^{\alpha}_{\vdash}\right)\upsilon^{\alpha}\, \mathrm{d}V - \int_P \left(\delta\dot{\rho}^{\alpha}_{\vdash}\,\mathrm{Div}\mathbf{s}^{\alpha}_r\right)\upsilon^{\alpha}\, \mathrm{d}V \; = 0. \tag{33}$$

Thus the elemental residual associated with the rate of dislocation density is expressed as

$$R^e_{\dot{\rho}_{\vdash}\alpha} = \sum_{i}^{\text{nodes}} R^{e\ i}_{\dot{\rho}_{\vdash}\alpha} = \sum_{i}^{\text{nodes}} \int \left(\mathbf{N}_l\dot{\rho}^{\alpha l}_{\vdash}\mathbf{N}_i - \upsilon^{\alpha}\left(\mathbf{s}^{\alpha}_r\cdot\mathbf{B}_i + \mathrm{Div}\mathbf{s}^{\alpha}_r\mathbf{N}_i\right)\right) \mathrm{d}V. \tag{34}$$

The elemental stiffness matrix $\mathbf{K}^e = \left[K^e_{\Gamma i \Lambda j} = \frac{\partial R^e_{\Gamma i}}{\partial \Lambda j}\right]$ and its components are calculated by imposing a low increment in nodal variables $\Delta\Lambda j$ and then calculation of variation of elemental residuals $\Delta R^e_{\Gamma i}$. The elemental residual and stiffness matrix are assembled over all elements as

$$\begin{bmatrix} K_{u\,u} & K_{u\,\dot{\rho}_{\vdash}\alpha} \\ K_{\dot{\rho}_{\vdash}\alpha\,u} & K_{\dot{\rho}_{\vdash}\alpha\,\dot{\rho}_{\vdash}\alpha} \end{bmatrix} \begin{bmatrix} du \\ d\dot{\rho}_{\vdash}\alpha \end{bmatrix} = - \begin{bmatrix} R_u \\ R_{\dot{\rho}_{\vdash}\alpha} \end{bmatrix}. \tag{35}$$

4 Results

In this section, the capability of the two-dimensional version of the model in the prediction of a wide range of hardening behaviors as well as rate-dependent and scale-variation responses in a single crystal, is investigated. The effect of the dissipative gradient strengthening as a source of isotropic-hardening behavior which may show a portion of dissipative plastic work done during the deformation is also studied. Furthermore, directional plastic flows in predefined slip systems and accumulation of GNDs are distinctly observed in a single crystal under three different loading conditions. Effects of scale variation in expansion of directional flows and accumulation of GNDs are also studied and simply linked to the phenomenon ‘smaller is stronger’. Moreover, the effect of a distinctive feature in the model which explains the effect of distortion of crystal lattice in the reference

Table 1 Predefined slip systems, $\mathbf{s}^{\alpha}$ and $\mathbf{m}^{\alpha}$—constant vectors in the intermediate space

Slip-system number α	Relative orientation between $\mathbf{s}^{\alpha}$ and (1, 0)	Slip vector $\mathbf{s}^{\alpha}$	Normal slip plane vector $\mathbf{m}^{\alpha}$
1	30°	$(\sqrt{3}/2, 1/2)$	$(-1/2, \sqrt{3}/2)$
2	60°	$(1/2, \sqrt{3}/2)$	$(\sqrt{3}/2, -1/2)$
3	120°	$(-1)/2, \sqrt{3}/2$	$(\sqrt{3}/2, 1/2)$
4	−30°	$(\sqrt{3}/2, -1/2)$	$(1/2, \sqrt{3}/2)$

Table 2 A common set of material coefficients and modeling parameters

μ	λ	S_y	υ_0	d_0	q	D	L_1, L_2	S_0	m	$h\left(S^{\beta}\right)$	κ
76.9 GPa	115.3 GPa	200 MPa	1e-3 1/s	1e-4 1/s	1.0 –	1 μm	1 μm	90e4 MPa	0.08 –	400 MPa	0.5 –

In order to gain insight into the spirit of proposed model, modeling parameters vanish or vary in different case studies

Table 3 In loading scenarios (1–3), a single crystal which is discretized by 5180 elements and incorporates the predefined slip systems (Table 1) is considered

Loading scenarios	Displacement-loading condition	Slip systems taken from Table 1
1	Figure 1a	Two slip systems, $\alpha = 1, 4$
2	Figure 1b	Four slip systems, $\alpha = 1, 2, 3, 4$
3	Figure 1c	Four slip systems, $\alpha = 1, 2, 3, 4$

Different loading conditions are employed based on Fig. 1. A common set of material parameters and modeling coefficients are taken from Table 2. Here, a high magnitude of $S_0 = 100\text{e}7\,\text{MPa}$ is considered

Table 4 In the case studies (1–6), a single crystal which is discretized by 96 elements and incorporates all four slip systems detailed in Table 1, is considered

Case study	A complete form of the flow rule according to the following conditions is employed
1	Term (III) is not activated, $L_2 = 0$, $S^{\alpha} = S_y$, $\dot{S}^{\alpha} = 0$ and L_1 varies
2	Term (III) is activated, $S^{\alpha} = S_y$, $\dot{S}^{\alpha} = 0$, L_1 and L_2 vary
3	Term (III) is activated, $S^{\alpha} = S_y$, $\dot{S}^{\alpha} \neq 0$, $\begin{cases} \kappa = 0 \\ \kappa \neq 0 \end{cases}$
4	Term (III) is switched off, $L_2 = 0$, $\dot{S}^{\alpha} \neq 0$, $\kappa \neq 0$
	The results are compared with previous case studies to release the effect of Term (III)
5	Rate-sensitivity parameter m varies in a range of 0.08–0.4
6	Size of single crystal D varies in a range of 0.125–8 μm, $L_2 = L_1 = 1\,\mu\text{m}$

Case studies (1–5) are under a cyclic simple-shear loading and case study (6) is subjected to a large-strain simple-shear loading. A common set of material parameters and modeling coefficients are taken from Table 2. Term (I) in the flow rule detailed in Eq. (23) is active for all case studies and modeling parameters vanish or vary in different case studies

configuration is also investigated. First of all, a two-dimensional square single-crystal in a size of $D = 1\,\mu\text{m}$ is employed. In order to show the strength of the implementation method for a distinct observation of dislocation glides in different directions, four arbitrary slip systems in a variety of slip directions (Table 1) are incorporated into the crystal. Here, the grain boundary is idealized considering the concept of hard boundary introduced in Sect. 2.5. A surrounding boundary-layer with a thickness of 0.01 μm enforces the microscopically hard boundary condition via $\upsilon^{\alpha} = 0$. A common set of material coefficients and modeling parameters are given in Table 2. The parameters μ and λ are taken from a common material with an elastic modulus $E = 200\,\text{GPa}$ and a Poisson's ratio $\nu = 0.3$, other parameters are employed in an acceptable range. In order to gain insight into the spirit of the model, different loading conditions and case studies which are detailed in Tables 3, 4, are carried out. The modeling parameters in the flow rule Eqs. (24, 25) may vary or vanish in different case studies.

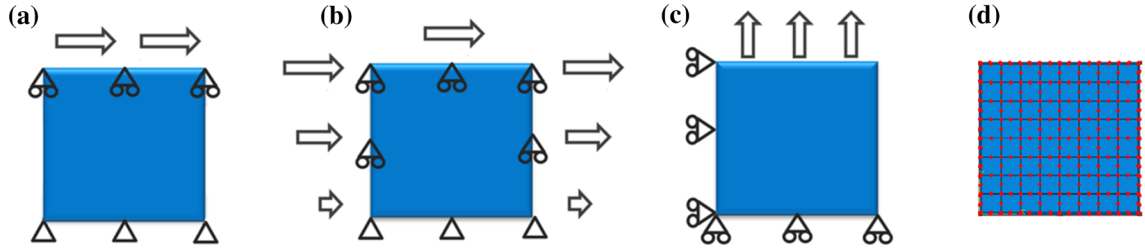

Fig. 1 Three different displacement-loading conditions are applied to the single crystal; **a** top surface is subjected to a horizontal displacement in the direction of (1, 0); **b** simple-shear loading; **c** tensile loading in the direction of (0, 1); **d** discretization with 96 elements, *red dots* represent nodes, each element is accompanied by 9 integration points (color figure online)

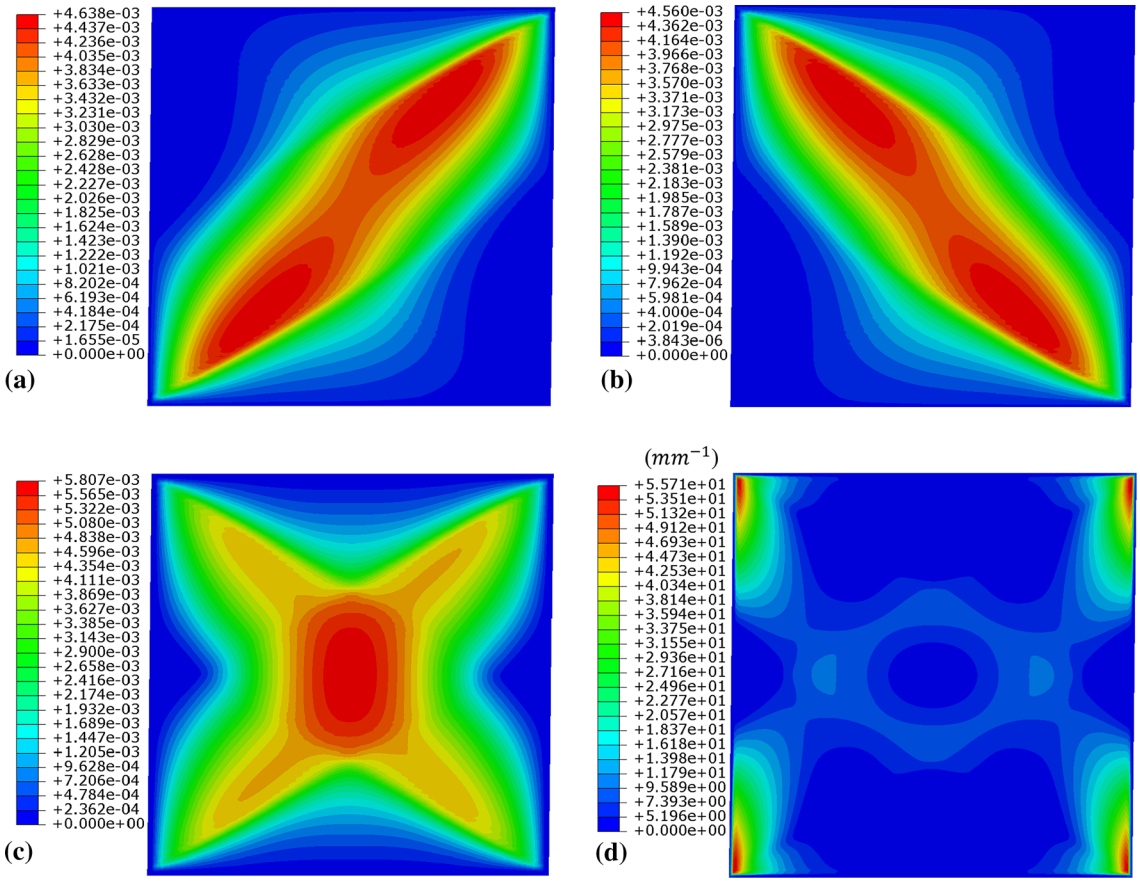

Fig. 2 Loading scenario (1), the single crystal at 1.1% strain via a loading condition depicted in Fig. 1a. **a**, **b** Contours of directional plastic flows $\int \upsilon^{\alpha} \mathrm{d}t$, respectively, for the predefined slip systems $\alpha = 1, 4$ (Table 1); **c** contour of a combination of plastic flows $\left(\sum_{\alpha} \left(\int \upsilon^{\alpha} \mathrm{d}t\right)^2\right)^{0.5}$; **d** contour of accumulation of dislocation densities $\left(\sum_{\alpha} \left(\int \dot{\rho}_{\perp}^{\alpha} \mathrm{d}t\right)^2\right)^{0.5}$

4.1 Different displacement-loading conditions

Loading scenarios (1, 2, 3) are detailed in Table 3. Here, it is aimed to distinctly observe directional plastic flows associated with the predefined slip systems as well as accumulation of GNDs in the single crystal. Three different displacement-loading conditions depicted in Fig. 1 are considered. Here, the single crystal is discretized by 5180 elements. A common set of material parameters and modeling coefficients given in Table 2 is employed. Here, a high magnitude of the energetic resistance $S_0 = 100e7\,\mathrm{MPa}$ is considered, which restrains expansion of plastic flows within the single crystal and provides us with a distinct observation of directional plastic flows as expected. Numerical results based on the loading scenarios (1–3) are illustrated in Figs. 2, 3 and 4, respectively. Plastic flow $\int \upsilon^{\alpha} \mathrm{d}t$ for each predefined slip direction, a combi-

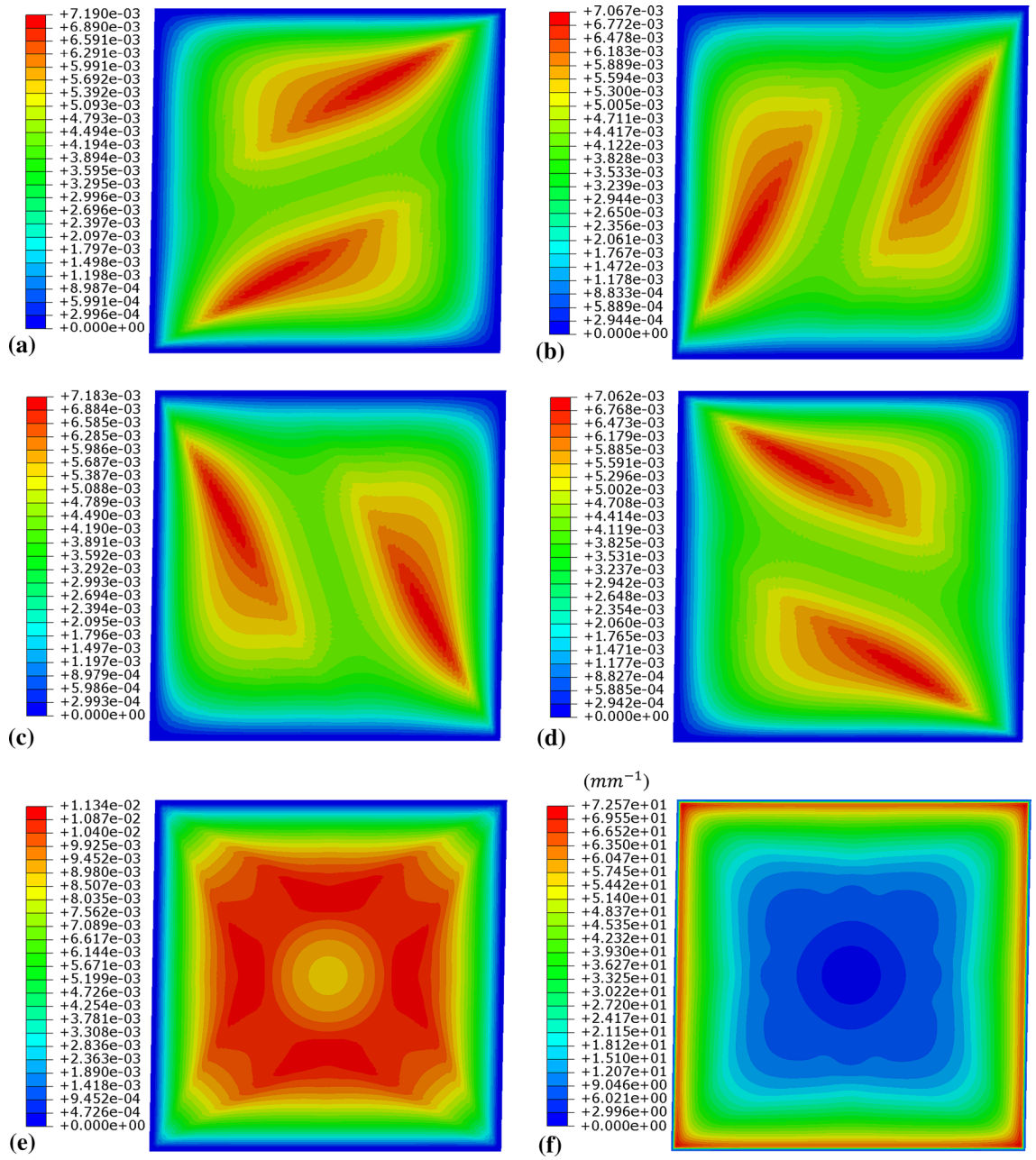

Fig. 3 Loading scenario (2), the single crystal at 1.6% strain via a loading condition depicted in Fig. 1b. **a**–**d** Contours of directional plastic flows $\int \upsilon^{\alpha} \mathrm{d}t$, respectively, for the predefined slip systems $\alpha = 1$–4 (Table 1); **e** contour of a combination of plastic flows $\left(\sum_{\alpha} \left(\int \upsilon^{\alpha} \mathrm{d}t\right)^2\right)^{0.5}$; **f** contour of accumulation of dislocation densities $\left(\sum_{\alpha} \left(\int \dot{\rho}_{\vdash}^{\alpha} \mathrm{d}t\right)^2\right)^{0.5}$

nation of all plastic flows $\left(\sum_{\alpha} \left(\int \upsilon^{\alpha} \mathrm{d}t\right)^2\right)^{0.5}$ and accumulation of edge dislocations $\left(\sum_{\alpha} \left(\int \dot{\rho}_{\vdash}^{\alpha} \mathrm{d}t\right)^2\right)^{0.5}$ are simply observed. Figures 2, 3 and 4 show that the plastic flows in an area close to the hard boundary are quite low and the edge dislocations are highly accumulated toward the boundary due to the hard boundary condition. In addition, directional plastic flows and accumulation of GNDs under a cyclic loading condition are investigated here. Figure 5 shows the stress–strain response of the single crystal under a cyclic version of loading scenario (2), four different red points: A, B, C and D which correspond respectively to strains $\varepsilon = 2, -0.67, -2$ and 0.16% are marked on the stress–strain curve. Figure 6 illustrates the directional plastic

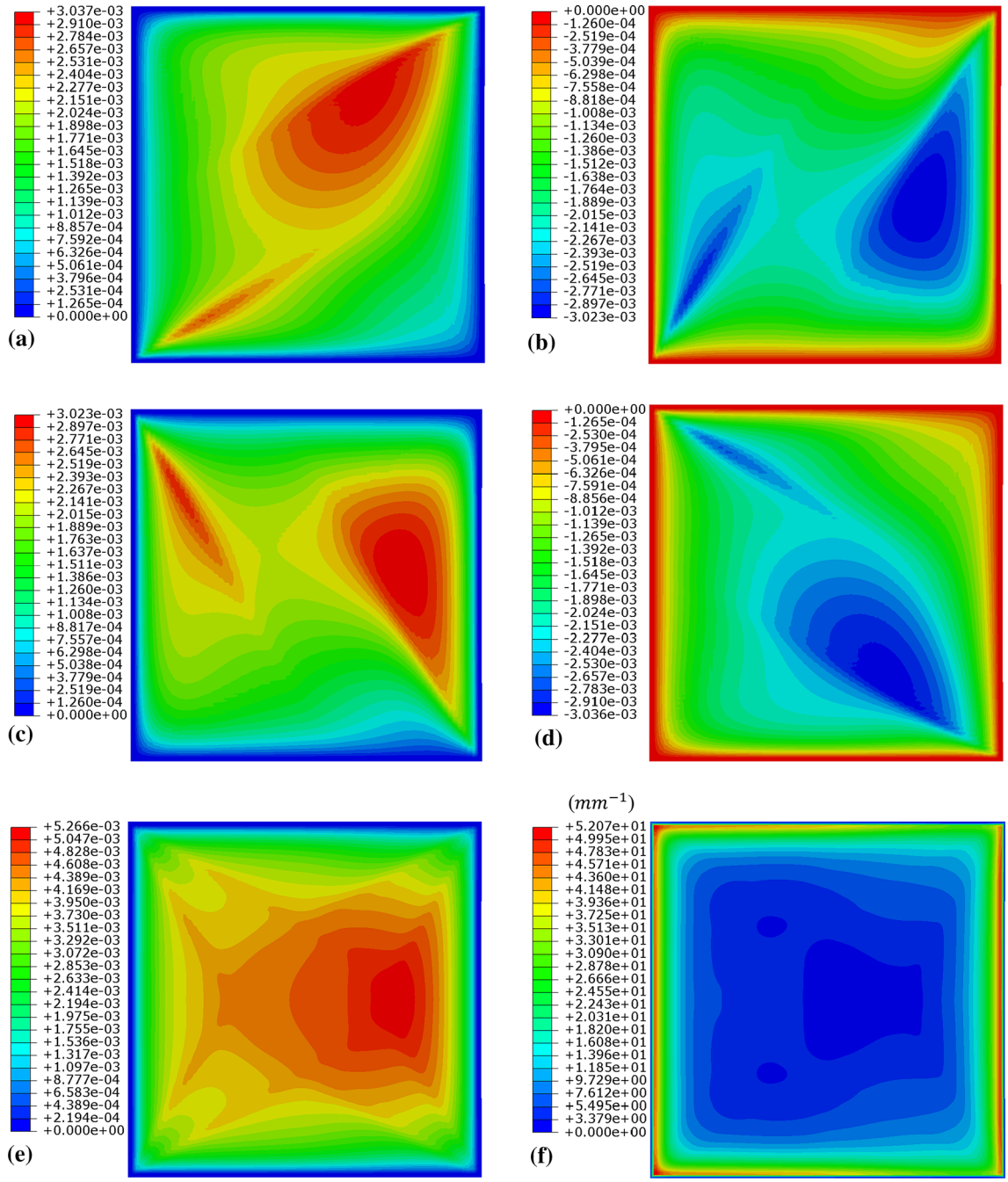

Fig. 4 Loading scenario (3), the single crystal at 0.6% strain via a loading condition depicted in Fig. 1c. **a**–**d** Contours of directional plastic flows $\int \upsilon^{\alpha} \mathrm{d}t$, respectively, for the predefined slip systems $\alpha = 1$–4 (Table 1); **e** contour of a combination of plastic flows $\left(\sum_{\alpha} \left(\int \upsilon^{\alpha} \mathrm{d}t\right)^2\right)^{0.5}$; **f** contour of accumulation of dislocation densities $\left(\sum_{\alpha} \left(\int \dot{\rho}_{\vdash}^{\alpha} \mathrm{d}t\right)^2\right)^{0.5}$

flow, a combination of plastic flows and accumulation of GNDs at different strains. Similar responses and behaviors are observed at points A and C. However, the directional plastic flows at A and C are, respectively, captured in positive and negative magnitudes as expected. Point B is located at the area of zero plastic flow (Fig. 5); therefore, very low plastic flows and accumulation of GNDs are observed at this point. Point D defines the single crystal at a positive strain location, although the directional plastic flow is observed in a negative magnitude.

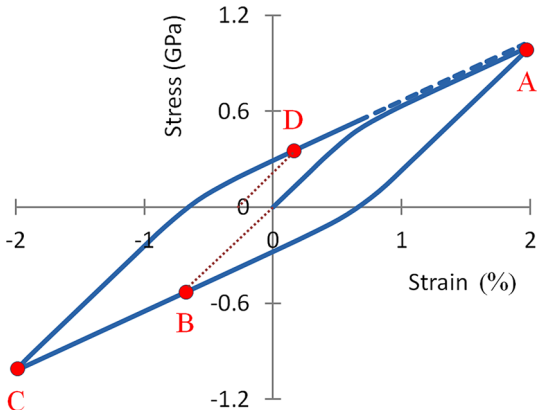

Fig. 5 The stress–strain response of the single crystal under a cyclic version of loading scenario (2). *Four different red points* A, B, C and D which correspond respectively to strains $\varepsilon = 2$, -0.67, -2 and 0.16 % are marked. A high magnitude of the energetic resistance $S_0 = 100e7$ MPa is considered here (color figure online)

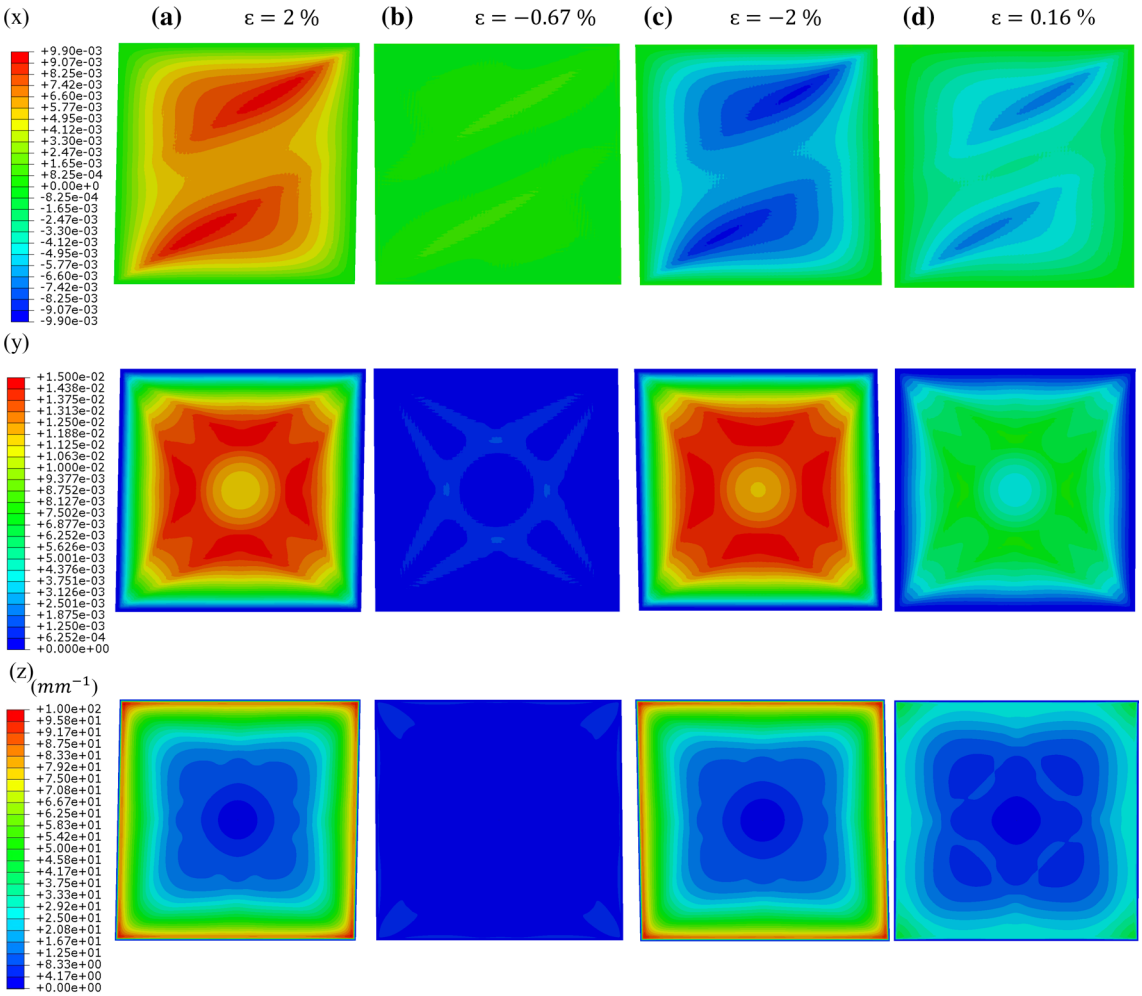

Fig. 6 A cyclic version of loading scenario (2) is applied to the single crystal. Numerical results corresponding to points **a**, **b**, **c** and **d** which have been marked on the stress–strain curve shown in Fig. 5, are presented. Row (x) contours of the directional plastic flow $\int \upsilon^{\alpha} \mathrm{d}t$ based on the predefined slip system $\alpha = 1$ (Table 1). Row (y) contour of a combination of plastic flows $\left(\sum_{\alpha} \left(\int \upsilon^{\alpha} \mathrm{d}t\right)^2\right)^{0.5}$, α = 1-4. Row (z) contour of accumulation of dislocation densities $\left(\sum_{\alpha} \left(\int \dot{\rho}^{\alpha}_{\vdash} \mathrm{d}t\right)^2\right)^{0.5}$. ε denotes the total strain (color figure online)

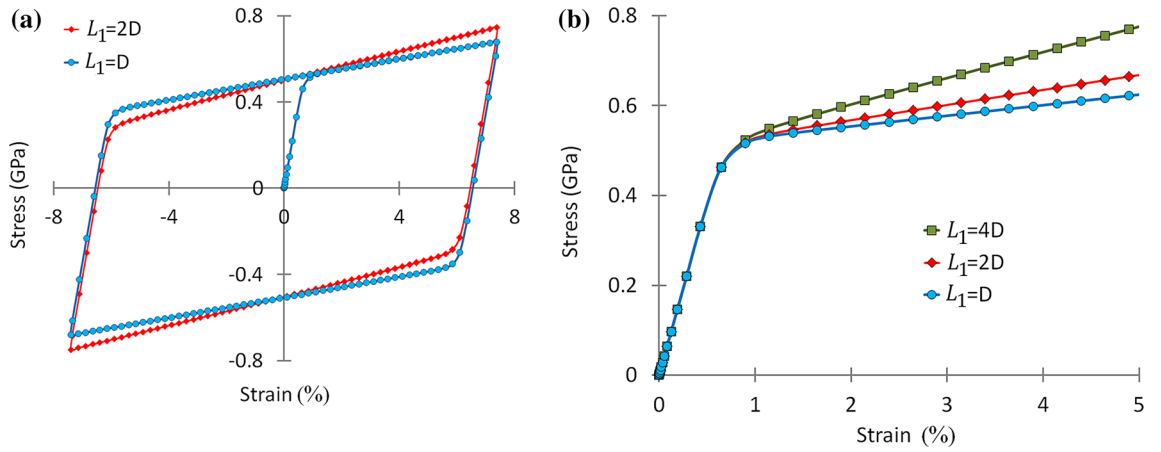

Fig. 7 A comparison of the stress–strain results obtained for different L_1/D ratios in the case study (1); $L_2 = 0$, $\dot{S}^{\alpha} = 0$. **a** The energetic gradient strengthening results in a kinematic-hardening behavior along with a Bauschinger-like response. **b** Changing in the energetic length-scale L_1 has no effect on the onset of plastic flow

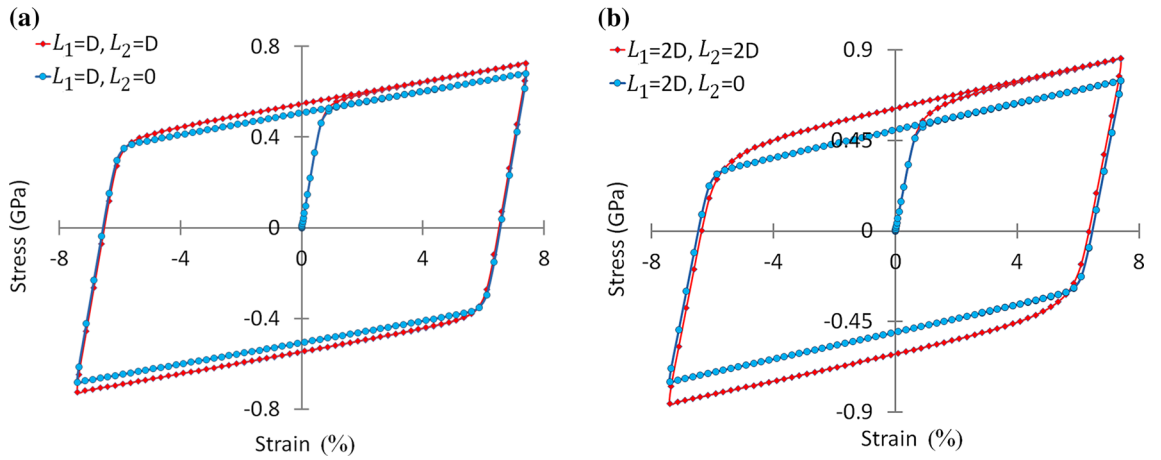

Fig. 8 A comparison of the stress–strain results obtained for different L_1/D and L_2/D ratios in the case study (2) along with $\dot{S}^{\alpha} = 0$. The dissipative gradient strengthening induces an increase in the yield strength

4.2 Different case studies

Case studies (1–6) are detailed in Table 4. In the case studies (1–5), the capability of the two-dimensional version of the model Eq. (25) in the prediction of a wide range of rate-dependent hardening behaviors via simulation of the single crystal under a cyclic simple-shear loading, is studied. Figure 1b depicts the simple-shear loading. In a similar vein with effect of irrecoverable work [83], the case study (4) investigates the dissipative gradient strengthening as a source of isotropic-hardening behavior which may represent a portion of dissipative plastic work which is associated with the long-range stress field. The case study (6) aims to validate the phenomenon 'smaller is stronger' in the single crystal under a large-strain simple-shear loading. In the case studies (1–6) discretization of single crystal by 96 elements results in a reasonable range of mesh-size insensitivity response along with an efficient calculation time. A study of mesh-size sensitivity can be found in "Appendix".

- Case study (1): $L_2 = 0$, $S^{\alpha} = S_y$ and $\dot{S}^{\alpha} = 0$. The effect of energetic gradient strengthening [term (I) in Eq. (25)] is studied here. The dissipative gradient strengthening [term (III)] is not involved and only the initial coarse-grain yield-threshold S_y is considered. Different L_1/D ratios are also employed. Figure 7a shows the effect of term (I) in the stress–strain responses, it can be concluded that the energetic gradient strengthening represents the kinematic hardening which is accompanied by a Bauschinger-like phenomenon. It is worth mentioning that GND densities which are evolved via the directional gradient of

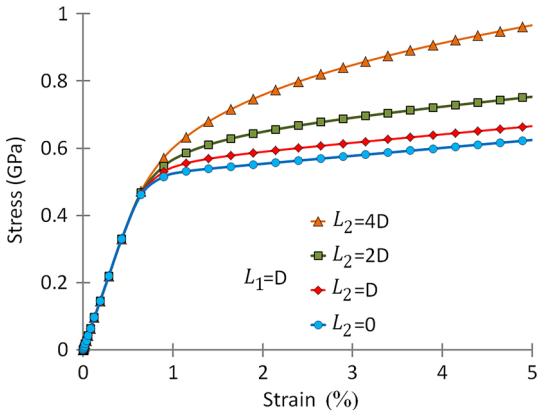

Fig. 9 A comparison of the stress–strain results obtained for different L_2/D ratios in the case study (2) along with $\dot{S}^\alpha = 0$. An increase in the dissipative length-scale L_2 changes the yield strength in the onset of plastic flow

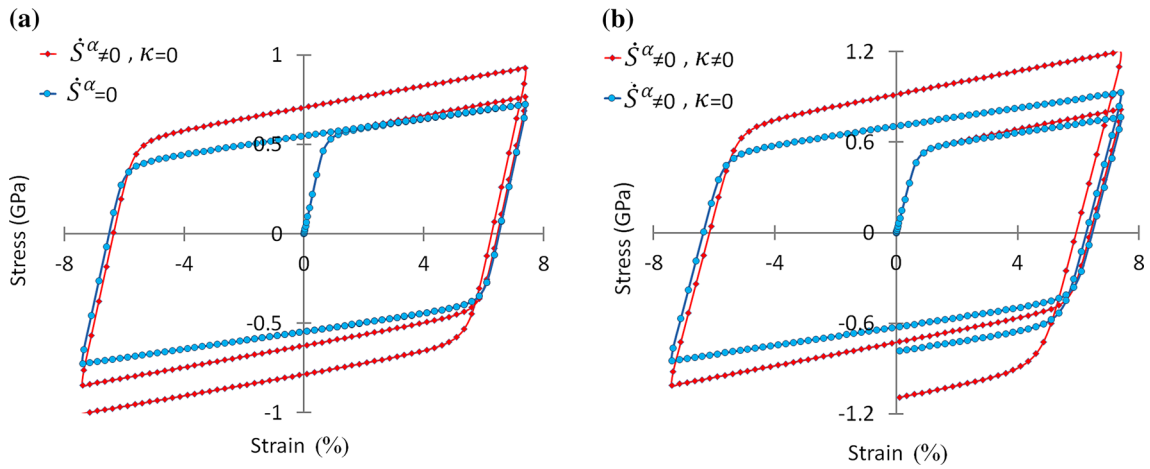

Fig. 10 A comparison of stress–strain results obtained for $L_1 = L_2 = D$ in the case study (3); **a** effect of the dissipative self-hardening ($\dot{S}^\alpha \neq 0, \kappa = 0$), and the result for $\dot{S}^\alpha = 0$ is taken from Fig. 8a; $L_1 = L_2 = D$, **b** effect of the dissipative latent-hardening ($\dot{S}^\alpha \neq 0$), $\kappa \neq 0$. The isotropic-hardening behavior is simply observed via employing the self- and latent-hardening

slip-rates (Sect. 2.2) are independent of sign of υ^α. Therefore, term (I) plays a role of energetic back-stress. Figure 7b shows that changing in the energetic length-scale L_1 has no effect on the onset of plastic flow. However, a higher strain-hardening response is observed with a larger value of L_1.

- Case study (2): $S^\alpha = S_y$, $\dot{S}^\alpha = 0$, and L_1/D and L_2/D vary. Effect of the dissipative gradient strengthening [term (III)] is investigated here. Figure 8 shows the stress–strain results. It can be seen that the dissipative gradient strengthening represents the yield strengthening. In order to gain insight into the effect of dissipative length-scale L_2, a varying L_2/D ratio along with $L_1 = D$ are considered here. Figure 9 shows that an increase in L_2 yields a higher yield strength in the onset of plastic flow which is in contrast to the response observed from the energetic length-scale in Fig. 7b. Bear in mind that $\dot{S}^\alpha = 0$ is considered here; thus, the post-yield strain-hardening is not induced. The effect of $\dot{S}^\alpha \neq 0$ in term (III) is studied in the case study (4).
- Case study (3): $\dot{S}^\alpha \neq 0$. Evolution of self- and latent-hardening is activated here. First, only self-hardening without latent one is considered ($\dot{S}^\alpha \neq 0, \kappa = 0$). Figure 10a shows the effect of self-hardening in the stress–strain results, it can be seen that self-hardening is a source of isotropic-hardening behavior and yields a post-yield strain-hardening response that consistently increases by plastic work. Second, the latent-hardening is taken into account ($\dot{S}^\alpha \neq 0, \kappa \neq 0$). Figure 10b indicates a comparison of stress–strain results obtained by considering self- and latent-hardening with the results obtained without latent-hardening (Fig. 10a). An additional isotropic-hardening response is easily observed via employing the latent-hardening. It is worth mentioning that self- and latent-hardening are evolved via ϕ^β in Eq. (17)

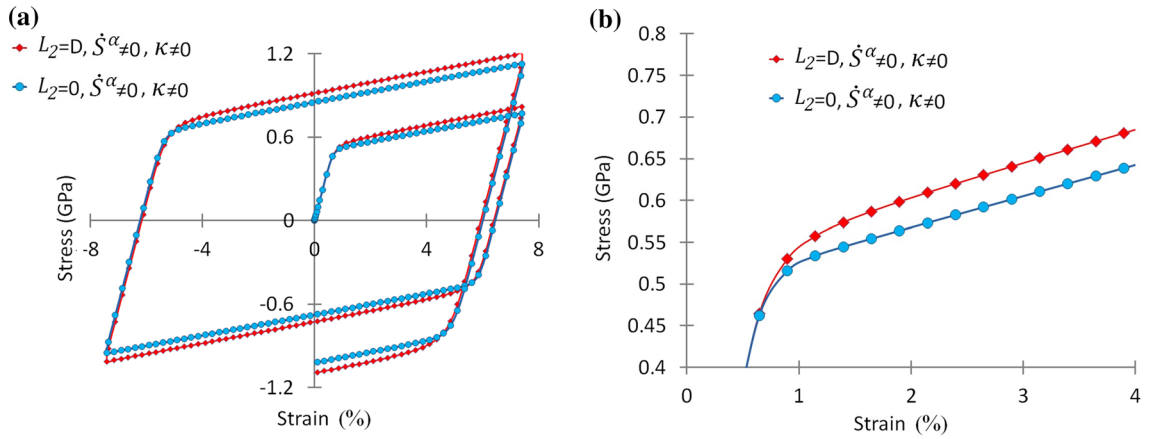

Fig. 11 **a** A comparison of the stress–strain result obtained in the case study (4) with a result taken from Fig. 10b—$L_2 = D$, $\dot{S}^{\alpha} \neq 0, \kappa \neq 0$. **b** Results in the area of onset of plastic flow. Considering the dissipative gradient strengthening [term (III)] gives rise to an additional isotropic-hardening behavior as well as a yield-strengthening response which has been already observed in the case study (2)

which is a function of accumulation rates of SSDs and GNDs [Eq. (18)]. Evers [78] emphasized that evolution of SSDs during crystallographic slips increases formation of short-range interactions between all dislocations, i.e., both SSDs and GNDs. These interactions turn to impede the dislocation movements and yield the isotropic-hardening responses which are observed in this case study.

- Case study (4), Gurtin and Ohno [83] proposed a new small-deformation gradient crystal-plasticity model which incorporates an irrecoverable stored energy of cold work and represents a new form of irrecoverable microstress and irrecoverable gradient strengthening [Eq. (13.5-6) in [83]]. Gurtin emphasized that the irrecoverable stored energy may lead to isotropic hardening which is induced via the new form of irrecoverable gradient strengthening. Moreover, the dissipative microstress which is introduced in the current large-deformation theory plays the same role as the new form proposed in the small-deformation model [83]. Gurtin highlighted that there is no way of differentiating between the new model and a theory in which the irrecoverable stored energy vanishes and a dissipative term is considered. Motivated by this statement, an isotropic-hardening response due to the dissipative gradient strengthening [term (III)] is also investigated. A complete form of Eq. (25) with $\dot{S}^{\alpha} \neq 0$ and $\kappa \neq 0$ is considered. Figure 11 compares the stress–strain responses obtained for $L_2 = 0$ with the result taken from Fig. 10b ($L_2 = D$, $\dot{S}^{\alpha} \neq 0, \kappa \neq 0$). Based on the results presented in Fig. 11, the dissipative gradient strengthening [term (III)] results in a yield-strengthening response (Fig. 11b) which has been already observed in the case study (2), as well as an isotropic-hardening behavior due to $\dot{S}^{\alpha} \neq 0$ in term (III) seen in Fig. 11a. It could be concluded that the isotropic-hardening behavior observed in the case study (3), Fig. 10b ($\dot{S}^{\alpha} \neq 0, \kappa \neq 0$), is induced by the evolution of short-range interactions, i.e., $\phi^{\beta} \neq 0$ in terms (II, III). The portion of isotropic hardening which is governed by the long-range stress filed $\boldsymbol{\xi}^{\alpha}_{\text{dis}}$ is quite of interest in the study of irrecoverable gradient works based on a gradient crystal-plasticity framework.
- Case study (5), two rate-sensitivity parameters m, q are employed in Eq. (23). Effect of m which is widely used in the conventional viscoplasticity and supposed to be quite small in simulation of metals under quasi-static loading, is studied here. Note that term (III) in Eq. (23) is simplified via $q = 1$ in Eq. (25). Figure 12a, b compares the stress–strain responses obtained based on a complete form of Eq. (25) and the coefficients and parameters detailed in Table 2 along with varying value of m. It can be concluded that considering $m = 0.08$ in this study, results in a low rate-dependent response. Figure 12a, b shows that an increase in m value in a range of greater than 0.12 results in a significant change in the onset of plastic flow and the post-yield response. Figure 12c, d compare the contribution of governing terms (I–III) at $m = 0.08$, 0.2. The change induced by m and $\dot{S}^{\alpha} \neq 0$ is quite significant in the contribution of term (II). A sharper rise in the contribution of term (III) (data set C) at the onset of plastic flow and at the area of strains below 2% can be also seen for lower m.
- Case study (6), employing all three governing components [terms (I–III)] in Eq. (25) with the common set of material coefficients and modeling parameters detailed in Table 2, yields a stress–strain response which shows a combination of isotropic and kinematic-like hardening behaviors as well as yield strengthening.

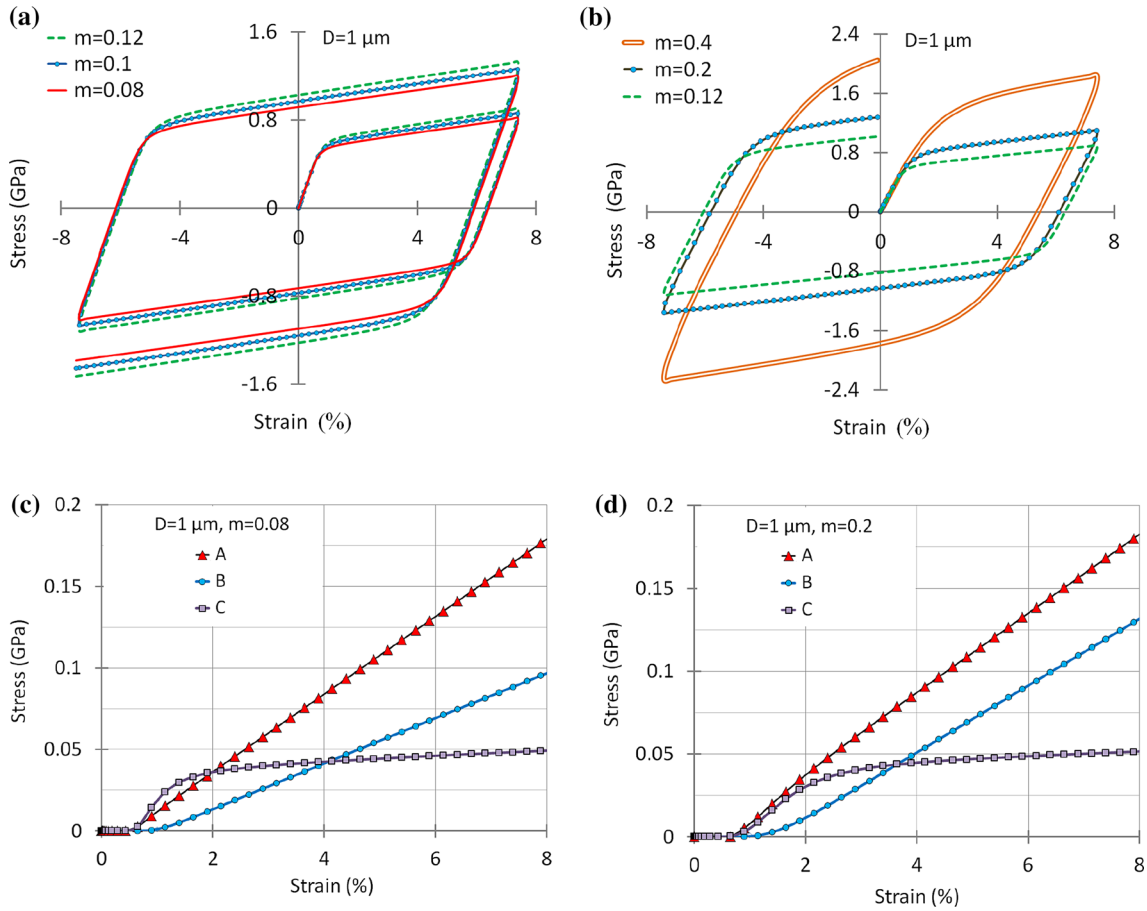

Fig. 12 **a**, **b** A comparison of rate-dependent stress–strain results obtained in the case study (5) for crystal size $D = 1\,\mu$m. Considering $m = 0.08$ results in a low rate-dependent response, and an increase in m value in a range of greater than 0.12 results in a significant change in the onset of plastic flow and the post-yield behavior. **c**, **d** A comparison of contribution of the governing terms (I–III) at $m = 0.08, 0.2$. *A* and *C* represent the effect of terms (I) and (III), and *B* shows the effect of m and $\dot{S}^{\alpha} \neq 0$ in term (II), beyond perfect plastic response. A change in data set *B* is quite clear. A sharper rise in the contribution of term (III) (data set *C*) at the onset of plastic flow is also seen for lower m

In this case study, a phenomenon which is so-called 'smaller is stronger' and refers to an increase in strengthening response with decrease in the crystal size, is investigated. A complete form of the flow rule Eq. (25) is employed to investigate size-dependent behavior of single crystals which are simulated with different crystal sizes D under a large-strain simple-shear loading. Figure 13a, b shows the stress–strain responses and indicate that the onset of plastic flow and the post-yield behavior are highly size-dependent. However, in a range of crystal size close to $8\mu m$, where $L_1/D = L_2/D = 0.125$, a nearly size-independent response is observed, and it can be concluded that the effect of gradient strengthenings [terms (I, III)] is insignificant in this range. Moreover, Fig. 13c, d compares the contribution of governing terms (I–III) at $D = 1$ and $0.25\,\mu$m. A size-dependent change in three governing terms is quite clear. In order to capture the variation of size dependency at different magnitude of rate-sensitivity parameter m, the size-dependent stress–strain responses at two different crystal sizes $D = 1$ and $0.25\,\mu$m are compared when $m = 0.08$ and 0.2. Figure 14 shows the size- and rate-dependent stress–strain responses. In the range of strains and in the resolution of results obtained in this study, it could be concluded that the size dependency of stress–strain response at a specific small strain is more pronounced at lower m, i.e., $\Delta 4 > \Delta 3$ and $\Delta 2 > \Delta 1$ in Fig. 14a. It is worth mentioning that by a lower m, a higher rate of flow at the onset plastic deformation is expected, which results in a sharper rise in the effect of gradient of plastic flow close to hard boundaries. Such a sharper rise can be observed in the contribution of term (III) (data set C) in Fig. 14c, e at lower m. In Fig. 14a, $\Delta 0 > \Delta 1$ compares the size dependency between two sets of points which are indicated via 0.2%-strain offset of elastic response guided by a green dash-line. At large enough strains, the size

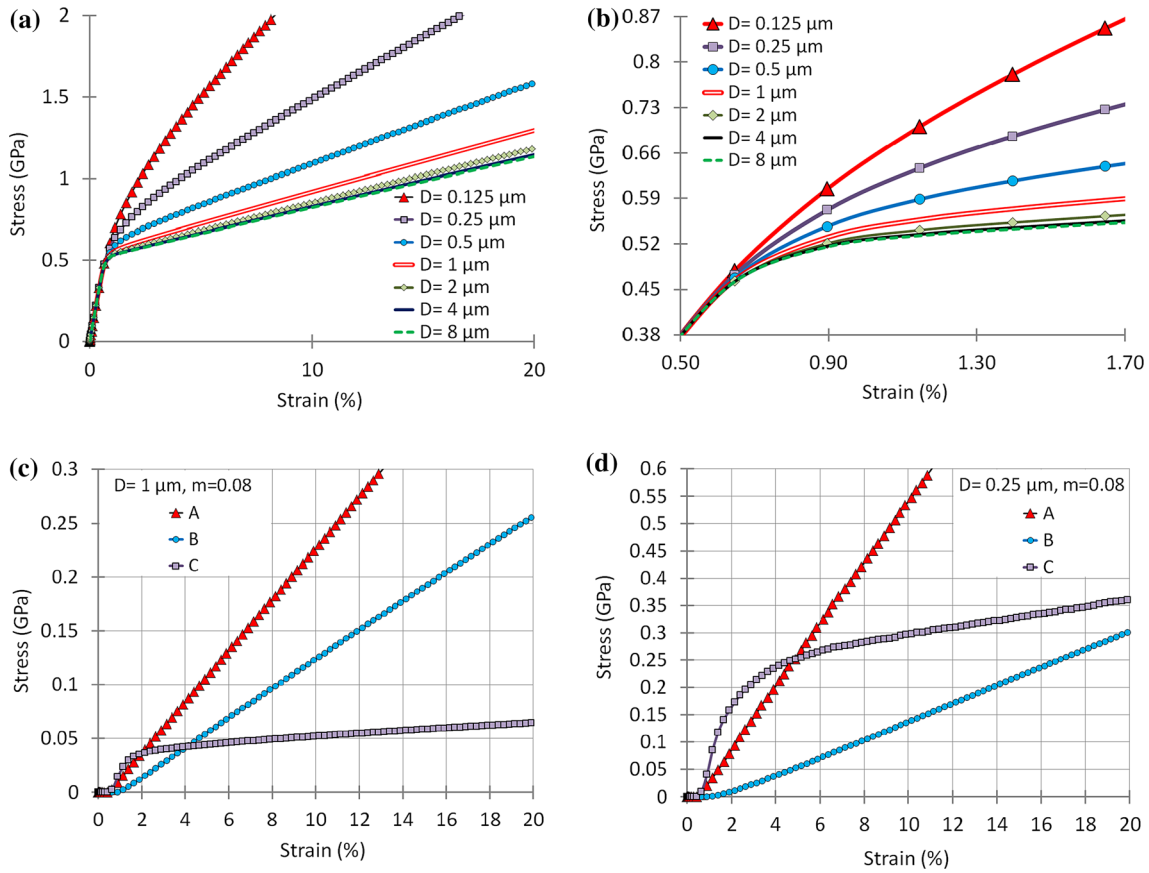

Fig. 13 **a** Size-dependent stress–strain responses obtained for $L_1 = L_2 = 1\,\mu$m in the case study (6), single crystals are simulated with different crystal sizes D at constant m =0.08; **b** results are distinctly shown in the area of onset of plastic flow. The post-yield behavior and the onset of plastic flow are clearly size-dependent. The phenomenon 'smaller is stronger' is simply observed. **c**, **d** A comparison of contribution of the governing terms (I–III) for $D = 1, 0.25\,\mu$m. A and C represent the effect of terms (I) and (III), and B shows the effect of $\dot{S}^{\alpha} \neq 0$ in term (II), beyond perfect plastic response. A size-dependent change in three data sets (A, B and C) is quite clear

dependency is greater by a higher m, i.e., $\Delta 5 > \Delta 6$ and $\Delta 7 > \Delta 8$ in Fig. 14b. It might be of interest to study an effect of grain size in the rate dependency of stress–strain responses in a wide range of strain rates, particularly at very low strain rates ($m \sim 0.01$). It is envisaged that a version of current model calibrated with a new set of modeling parameters at low strain rates could capture such a grain-size dependency of rate-dependence response which has been reported in i.e., [95].

4.3 Effect of scale variation in directional plastic flows and accumulation of GNDs

In order to observe the effect of scale variation in directional plastic flows and accumulation of GNDs, loading scenario (2) is recalled and applied to two more single crystals with different crystal sizes $D = 0.5$ and $2\,\mu$m. Figure 15 compares the numerical results obtained here with the results presented in Fig. 3 for a single crystal with $D = 1\,\mu$m. A high magnitude of the energetic resistance $S_0 = 100e7$ MPa is considered here. Based on the results depicted in Fig. 15-rows a, b, it can be concluded that an increase in the crystal size results in a larger magnitude of plastic flows as well as a more expansion of plastic flows toward the boundary. Smaller crystals show a higher aggregation of plastic flows toward the center of crystals. Results presented in Fig. 15-row c indicate the greatest magnitude of GND density (dislocations pile-up) in an area close to the hard boundary. It can also be concluded that a decrease in the crystal size yields an increase in the accumulation of GNDs toward the boundary. A smaller crystal shows a more expansive accumulation of GNDs and is subjected to a larger value of gradient strengthening; thus, the phenomenon 'smaller is stronger' is validated.

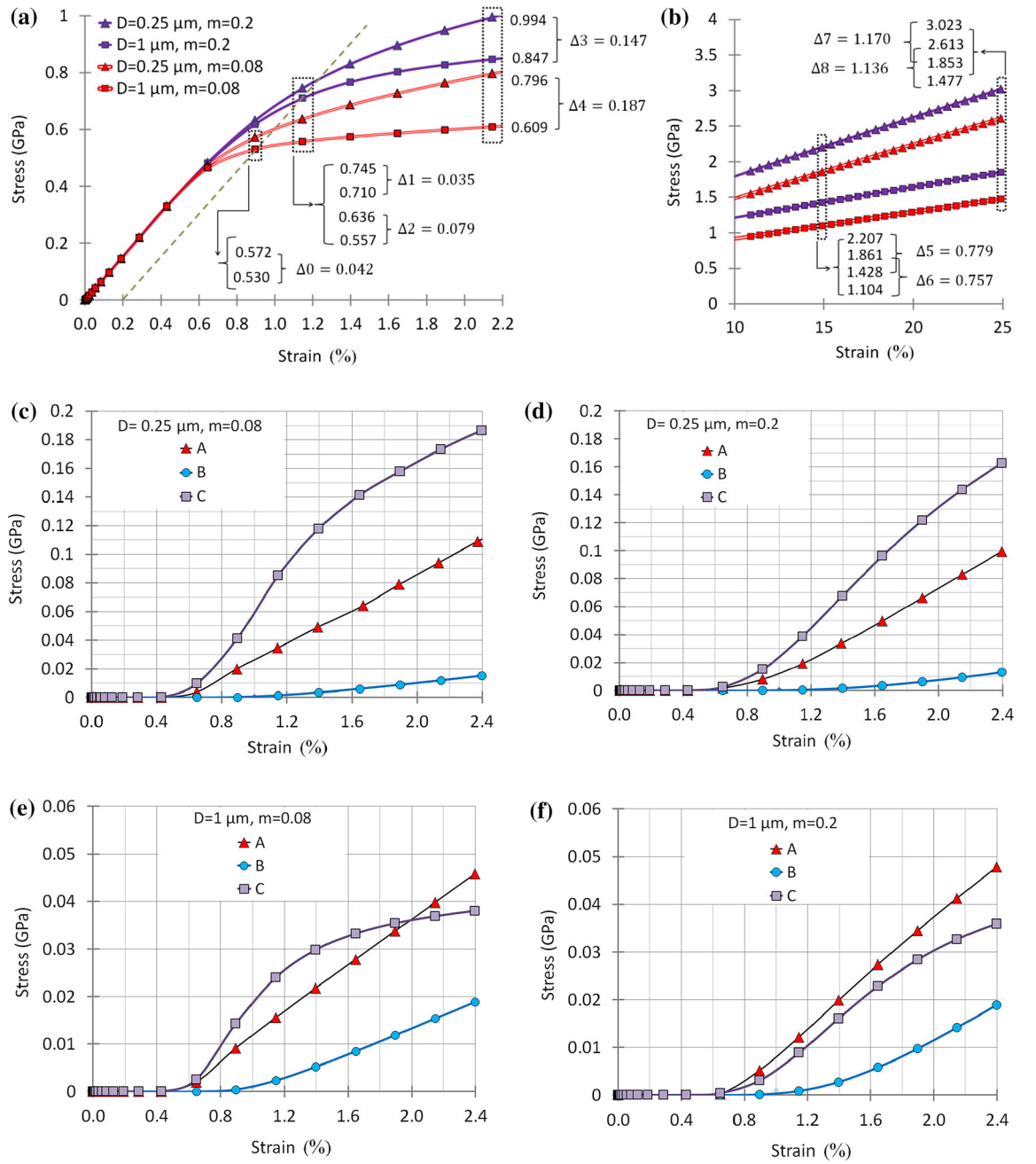

Fig. 14 Size- and rate-dependent stress–strain responses obtained for $L_1 = L_2 = 1\,\mu$m in the case study (6), single crystals are simulated with different crystal sizes $D = 1$ and $0.25\,\mu$m at $m = 0.08$ and 0.2. **a**, **b** Four sets of points at different fixed strains are indicated with *boxes*. The values denote the stress magnitudes at points. $\Delta 0$–8 represent changes in the stress magnitudes. The *green dash-line* indicates a 0.2%-strain offset of elastic response. **a** Here, $\Delta 4 > \Delta 3$ and $\Delta 2 > \Delta 1$ denote that a change in the size-dependent stress–strain response at a specific small strain is more pronounced at lower m. **b** At large enough strains, the size dependency is greater by a higher m, i.e., $\Delta 5 > \Delta 6$ and $\Delta 7 > \Delta 8$. **c**, **f** The contribution of the governing terms (I–III) corresponding to the stress–strain response shown in (**a**). *A* and *C* represents the effect of terms (I) and (III), and *B* shows the effect of m and $\dot{S}^{\alpha} \neq 0$ in term (II), beyond perfect plastic response (color figure online)

4.4 Effect of distortion of crystal lattice

Here, the effect of a distinctive feature (Div $\mathbf{s}_r^{\alpha}$) in Gurtin's finite-deformation gradient crystal-plasticity theory which explains the effect of distortion of crystal lattice in the reference configuration [Eq. (4) and the following

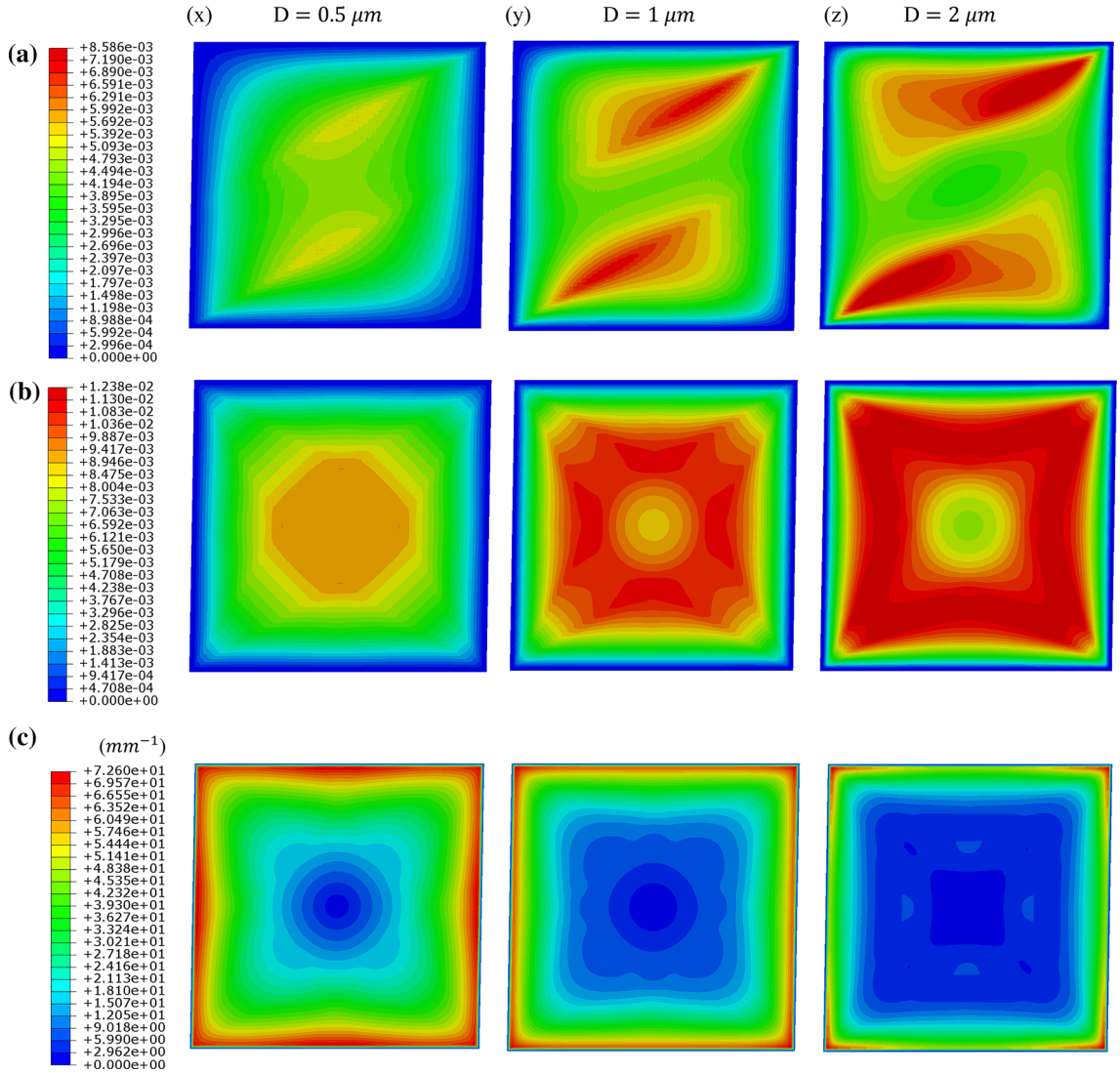

Fig. 15 Loading scenario (2) detailed in Table 3 is applied to three different single crystals with different crystal sizes (D). Numerical results corresponding to 1.6% shear strain are presented. Columns (x, y, z) represent the results obtained for $D = 0.5$, 1 and 2 μm, respectively. Row **a** Contours of the directional plastic flow $\int \upsilon^{\alpha} \mathrm{d}t$ based on the predefined slip system $\alpha = 1$ (Table 1). Row **b** contour of a combination of plastic flows $\left(\sum_{\alpha} \left(\int \upsilon^{\alpha} \mathrm{d}t\right)^2\right)^{0.5}$, α = 1-4. Row **c** contour of accumulation of dislocation densities $\left(\sum_{\alpha} \left(\int \dot{\rho}_{\vdash}^{\alpha} \mathrm{d}t\right)^2\right)^{0.5}$ (color figure online)

paragraph] is investigated. It is worth noting that evaluation of Div $\mathbf{s}_r^{\alpha}$ and Div $\left(\mathbf{s}_r^{\alpha} / \left|\mathbf{s}_r^{\alpha}\right|^2\right)$ represented in Eqs. (26, 34) requires an intricate analysis at the integration points, which is time consuming and cannot be simply accomplished via a user-defined subroutine (UEL). A discussion on the evaluation of these terms has been presented in a study by Kuroda [70].[5] However, the effect of Div $\mathbf{s}_r^{\alpha}$ was not successfully captured in [70] in the resolution of plots reported. In the current study, Div $\boldsymbol{\varphi}$ where $\boldsymbol{\varphi}$ is a vector, is evaluated via a common block function which is linked to UEL subroutine. The components of $\boldsymbol{\varphi}$ at integration points are extrapolated to nodes. An averaging method at each node combines the vector's components provided from neighboring elements, then Div $\boldsymbol{\varphi}$ is calculated at integration points within each elements. The effect of Div $\mathbf{s}_r^{\alpha}$ and Div $\left(\mathbf{s}_r^{\alpha} / \left|\mathbf{s}_r^{\alpha}\right|^2\right)$ in Eqs. (26, 34) is investigated here. Figure 16 compares three sets of results taken from

[5] The model employed in Kuroda [70] is based on the study by Kuroda and Tvergaard [69] and does not incorporate the dissipative microstress, the gradient yield-strengthening and the dissipative length-scale.

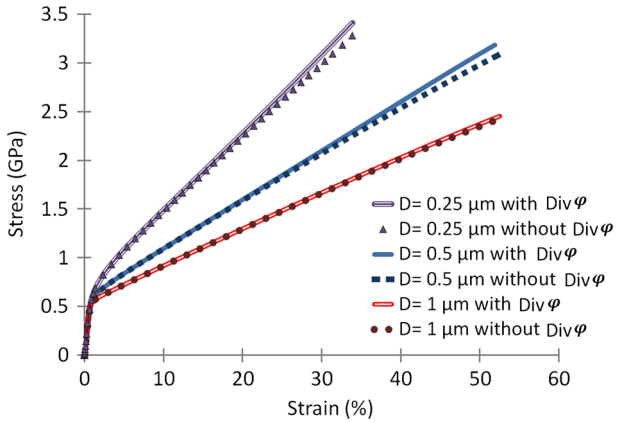

Fig. 16 Three sets of results (*solid lines*) taken from Fig. 13a, which correspond to the response of single crystals under the large-strain simple-shear loading, are compared with three sets of responses of same single crystals obtained when Div $\boldsymbol{\varphi}$ vanishes in the constitutive model. $\boldsymbol{\varphi}$ represents $\mathbf{s}_r^\alpha$ and $\mathbf{s}_r^\alpha / \left|\mathbf{s}_r^\alpha\right|^2$

Fig. 13a, which correspond to the response of single crystals under the large-strain simple-shear loading, with three other sets of responses of same single crystals obtained when Div $\mathbf{s}_r^\alpha$ and Div $\left(\mathbf{s}_r^\alpha / \left|\mathbf{s}_r^\alpha\right|^2\right)$ vanishes in the constitutive model. Based on the modeling parameters and coefficients employed in this study, it can be concluded from Fig. 16 that Div $\mathbf{s}_r^\alpha$ and Div $\left(\mathbf{s}_r^\alpha / \left|\mathbf{s}_r^\alpha\right|^2\right)$ together play the effective role in large strains, and it is more pronounced when the crystal size decreases and a higher degree of gradient strengthening is experienced.

5 Summary and conclusion

The comprehensive study represented in the current work confirms the strength of the finite-deformation gradient crystal-plasticity framework proposed by Gurtin [51] in order to distinctly describe a wide range of hardening behaviors as well as rate-dependent and scale-variation responses in single crystals. The framework was revisited first with respect to the reference configuration to facilitate the numerical implementation. The numerical results reveal that the energetic and dissipative gradient strengthenings yield, respectively, the kinematic-hardening behavior and yield-strengthening response. It is also concluded that the dissipative and energetic length-scales act differently; the former affects the onset of plastic flow, and the latter results in a change of the post-yield strain-hardening response. Moreover, the evolution of self- and latent-hardening is induced via a function of accumulation rates of SSDs and GNDs which represents a measure of formation of short-range interactions between SSDs and GNDs. These interactions turn to impede the dislocation movements and yield isotropic-hardening responses. The simulation results reveal that the dissipative gradient strengthening can be identified as a source of isotropic-hardening behavior and may represent a portion of dissipative plastic work which is associated with the long-range stress field. Furthermore, the effect of a distinctive feature in Gurtin's finite-deformation gradient crystal-plasticity framework which explains the effect of distortion of crystal lattice in the reference configuration was observed in this study for the first time. In addition, the rate-dependent stress–strain response of single crystals is reported, and the directional plastic flows and accumulation of GNDs toward the hard boundary are distinctly observed in a single crystal under three different loading conditions. Furthermore, the phenomenon 'smaller is stronger' is easily validated in different crystal sizes, smaller crystals show a more expansive accumulation of GNDs along with a larger value of gradient strengthening, and larger crystals present a larger magnitude of plastic flows as well as a more expansion of plastic flows toward the boundary. It has been also seen that the size dependency is more pronounced at a fixed small strain when the rate-sensitivity parameter m is lower. At large enough strains, the size dependency is greater by a higher m.

Finally, the current model can predict a wide variety of behaviors and responses of single crystals which have been already observed in experiments and it is envisaged that current work may provide a profound understanding of gradient crystal-plasticity theories in the finite-deformation framework.

Acknowledgements The support rendered by the German Research Foundation (DFG) for research Grant SFB 666 is cordially acknowledged.

Appendix

In the case studies (1–6), the single crystal is discretized by 96 elements (321 nodes and 864 integration points). Table 5 shows the magnitude of stress at a specific strain 7.4% during first cycle loading, when the number of elements is 96, 320 and 725. Here, the calculation time up to the strain 7.4% is also reported.

Table 5 The magnitude of stress at a specific strain 7.4% during first cycle loading, when the number of elements is 96, 320 and 725

Number of elements	96	320	725
Magnitude of stress	817 MPa	881 MPa	897 MPa
Calculation time	35 min	151 min	333 min

The calculation time up to the strain 7.4% is captured

References

1. Clayton, J.D.: Nonlinear Mechanics of Crystals, Solid Mechanics and Its Applications, vol. 177. Springer, Dordrecht (2011)
2. Hull, D., Bacon, D.J.: Introduction to Dislocations. Butterworth-Heinemann, Oxford (2011)
3. Hutchinson, J.W.: Plasticity at the micron scale. Int. J. Solids Struct. **37**, 225–238 (2000). doi:10.1016/S0020-7683(99)00090-6
4. Raabe, D., Sachtleber, M., Zhao, Z., Roters, F., Zaefferer, S.: Micromechanical and macromechanical effects in grain scale polycrystal plasticity experimentation and simulation. Acta Mater. **49**, 3433–3441 (2001). doi:10.1016/S1359-6454(01)00242-7
5. Maaß, R., Van Petegem, S., Ma, D., Zimmermann, J., Grolimund, D., Roters, F., Van Swygenhoven, H., Raabe, D.: Smaller is stronger: the effect of strain hardening. Acta Mater. **57**, 5996–6005 (2009). doi:10.1016/j.actamat.2009.08.024
6. Fleck, N.A., Muller, G.M., Ashby, M.F., Hutchinson, J.W.: Strain gradient plasticity: theory and experiment. Acta Metall. Mater. **42**, 475–487 (1994). doi:10.1016/0956-7151(94)90502-9
7. Hall, E.O.: The deformation and ageing of mild steel. 3. Discussion of results. Proc. Phys. Soc. Lond. B **64**, 747–753 (1951). doi:10.1088/0370-1301/64/9/303
8. Petch, N.J.: The cleavage strength of polycrystals. J. Iron Steel **I**(174), 25–28 (1953)
9. Yefimov, S., van der Giessen, E.: Size effects in single crystal thin films: nonlocal crystal plasticity simulations. Eur. J. Mech. A Solids **24**, 183–193 (2005). doi:10.1016/j.euromechsol.2005.01.002
10. Abu Al-Rub, R.K., Voyiadjis, G.Z.: Analytical and experimental determination of the material intrinsic length scale of strain gradient plasticity theory from micro- and nano-indentation experiments. Int. J. Plast. **20**, 1139–1182 (2004). doi:10.1016/j.ijplas.2003.10.007
11. Rice, J.R.: Inelastic constitutive relations for solids: an internal-variable theory and its application to metal plasticity. J. Mech. Phys. Solids **19**, 433–455 (1971). doi:10.1016/0022-5096(71)90010-X
12. Asaro, R.J., Rice, J.R.: Strain localization in ductile single crystals. J. Mech. Phys. Solids **25**, 309–338 (1977). doi:10.1016/0022-5096(77)90001-1
13. Teodosiu, C., Sidoroff, F.: A theory of finite elastoviscoplasticity of single crystals. Int. J. Eng. Sci. **14**, 165–176 (1976). doi:10.1016/0020-7225(76)90085-9
14. Aifantis, E.C.: Update on a class of gradient theories. Mech. Mater. **35**, 259–280 (2003). doi:10.1016/S0167-6636(02)00278-8
15. Fleck, N.A., Hutchinson, J.W.: Strain gradient plasticity. Adv. Appl. Mech. **33**, 295–361 (1997). doi:10.1016/S0065-2156(08)70388-0
16. Gudmundson, P.: A unified treatment of strain gradient plasticity. J. Mech. Phys. Solids **52**, 1379–1406 (2004). doi:10.1016/j.jmps.2003.11.002
17. Gurtin, M.E., Anand, L.: Thermodynamics applied to gradient theories involving the accumulated plastic strain: the theories of Aifantis and Fleck and Hutchinson and their generalization. J. Mech. Phys. Solids **57**, 405–421 (2009). doi:10.1016/j.jmps.2008.12.002
18. Nye, J.F.: Some geometrical relations in dislocated crystals. Acta Metall. **1**, 153–162 (1953). doi:10.1016/0001-6160(53)90054-6
19. Ashby, M.F.: Deformation of plastically non-homogeneous materials. Philos. Mag **21**, 399 (1970). doi:10.1080/14786437008238426
20. Gao, H., Huang, Y., Nix, W.D., Hutchinson, J.W.: Mechanism-based strain gradient plasticity—I. Theory. J. Mech. Phys. Solids **47**, 1239–1263 (1999). doi:10.1016/S0022-5096(98)00103-3
21. Nix, W.D., Gao, H.: Indentation size effects in crystalline materials: a law for strain gradient plasticity. J. Mech. Phys. Solids **46**, 411–425 (1998). doi:10.1016/S0022-5096(97)00086-0
22. Han, C.-S., Gao, H., Huang, Y., Nix, W.D.: Mechanism-based strain gradient crystal plasticity—I. Theory. J. Mech. Phys. Solids **53**, 1188–1203 (2005). doi:10.1016/j.jmps.2004.08.008
23. Steinmann, P.: Geometrical Foundations of Continuum Mechanics: An Application to First- and Second-Order Elasticity and Elasto-Plasticity. Lecture Notes in Applied Mathematics and Mechanics, vol. 2. Springer, Heidelberg (2015)
24. Naghdi, P.M., Srinivasa, A.R.: Some general results in the theory of crystallographic slip. Z. Angew. Math. Phys. **45**, 687–732 (1994). doi:10.1007/Bf00942749

25. Taylor, G.I.: The Mechanism of Plastic Deformation of Crystals. Part I. Theoretical. Proceedings of the Royal Society of London. Series A **145**, 362–387 (1934). doi:10.1098/rspa.1934.0106
26. Aifantis, E.C.: On the microstructural origin of certain inelastic models. J. Eng. Mater. Technol. Asme **106**, 326–330 (1984)
27. Zbib, H.M., Aifantis, E.C.: On the structure and width of shear bands in finite elastoplastic deformations. In: Boehler, J.-P., Khan, A. (eds.) Anisotropy and Localization of Plastic Deformation. Springer, Berlin (1991)
28. Aifantis, E.C.: The physics of plastic-deformation. Int. J. Plast. **3**, 211–247 (1987). doi:10.1016/0749-6419(87)90021-0
29. Toupin, R.A.: Elastic materials with couple-stresses. Arch. Ration. Mech. Anal. **11**, 385–414 (1962). doi:10.1007/BF00253945
30. Fleck, N.A., Hutchinson, J.W.: A phenomenological theory for strain gradient effects in plasticity. J. Mech. Phys. Solids **41**, 1825–1857 (1993). doi:10.1016/0022-5096(93)90072-N
31. Fleck, N.A., Hutchinson, J.W.: A reformulation of strain gradient plasticity. J. Mech. Phys. Solids **49**, 2245–2271 (2001). doi:10.1016/S0022-5096(01)00049-7
32. Fleck, N.A., Hutchinson, J.W.: Strain gradient plasticity. In: John, W.H., Theodore, Y.W. (eds.) Advances in Applied Mechanics. Elsevier, Amsterdam (1997)
33. Acharya, A., Bassani, J.L.: On non-local flow theories that preserve the classical structure of incremental boundary value problems. In: Pineau, A., Zaoui, A. (eds.) IUTAM Symposium on Micromechanics of Plasticity and Damage of Multiphase Materials. Springer, Berlin (1996)
34. Bassani, J.L.: Incompatibility and a simple gradient theory of plasticity. J. Mech. Phys. Solids **49**, 1983–1996 (2001). doi:10.1016/S0022-5096(01)00037-0
35. Cosserat, E., Cosserat, F.: Theorie des corps deformables. Librairie Scientifique A. Hermannet Fils, Paris (1909)
36. Mandel, J.: Equations constitutives et directeurs dans les milieux plastiques et viscoplastiques. Int. J. Solids Struct. **9**, 725–740 (1973). doi:10.1016/0020-7683(73)90120-0
37. Sedlacek, R., Forest, S.: Non-local plasticity at microscale: a dislocation-based and a Cosserat model. Phys. Status Solidi B **221**, 583–596 (2000). doi:10.1002/1521-3951(200010)221:2<583::Aid-Pssb583>3.0.Co;2-F
38. Forest, S.: Some links between Cosserat, strain gradient crystal plasticity and the statistical theory of dislocations. Philos. Mag. (2008). doi:10.1080/14786430802154815
39. Forest, S., Sedlacek, R.: Plastic slip distribution in two-phase laminate microstructures: dislocation-based versus generalized continuum approaches. Philos. Mag. **83**, 245–276 (2003). doi:10.1080/0141861021000022255
40. Svendsen, B.: Continuum thermodynamic models for crystal plasticity including the effects of geometrically-necessary dislocations. J. Mech. Phys. Solids **50**, 1297–1329 (2002). doi:10.1016/S0022-5096(01)00124-7
41. Menzel, A., Steinmann, P.: On the continuum formulation of higher gradient plasticity for single and polycrystals. J. Mech. Phys. Solids **48**, 1777–1796 (2000). doi:10.1016/S0022-5096(99)00024-1
42. Cermelli, P., Gurtin, M.E.: On the characterization of geometrically necessary dislocations in finite plasticity. J. Mech. Phys. Solids **49**, 1539–1568 (2001). doi:10.1016/S0022-5096(00)00084-3
43. Cermelli, P., Gurtin, M.E.: Geometrically necessary dislocations in viscoplastic single crystals and bicrystals undergoing small deformations. Int. J. Solids Struct. **39**, 6281–6309 (2002). doi:10.1016/S0020-7683(02)00491-2
44. Gurtin, M.E.: On the plasticity of single crystals: free energy, microforces, plastic-strain gradients. J. Mech. Phys. Solids **48**, 989–1036 (2000). doi:10.1016/S0022-5096(99)00059-9
45. Fried, E., Gurtin, M.E.: Continuum theory of thermally induced phase transitions based on an order parameter. Physica D Nonlinear Phenom. **68**, 326–343 (1993). doi:10.1016/0167-2789(93)90128-N
46. Fried, E., Gurtin, M.E.: Dynamic solid–solid transitions with phase characterized by an order parameter. Physica D Nonlinear Phenom. **72**, 287–308 (1994). doi:10.1016/0167-2789(94)90234-8
47. Gurtin, M.E., Fried, E., Anand, L.: The Mechanics and Thermodynamics of Continua. Cambridge University Press, New York (2010)
48. Gurtin, M.E.: A finite-deformation, gradient theory of single-crystal plasticity with free energy dependent on the accumulation of geometrically necessary dislocations. Int. J. Plast. **26**, 1073–1096 (2010). doi:10.1016/j.ijplas.2010.02.002
49. Lele, S.P., Anand, L.: A large-deformation strain-gradient theory for isotropic viscoplastic materials. Int. J. Plast. **25**, 420–453 (2009). doi:10.1016/j.ijplas.2008.04.003
50. Lele, S.P., Anand, L.: A small-deformation strain-gradient theory for isotropic viscoplastic materials. Philos. Mag. (2008). doi:10.1080/14786430802087031
51. Gurtin, M.E.: A finite-deformation, gradient theory of single-crystal plasticity with free energy dependent on densities of geometrically necessary dislocations. Int. J. Plast. **24**, 702–725 (2008). doi:10.1016/j.ijplas.2007.07.014
52. Gurtin, M.E., Anand, L., Lele, S.P.: Gradient single-crystal plasticity with free energy dependent on dislocation densities. J. Mech. Phys. Solids **55**, 1853–1878 (2007). doi:10.1016/j.jmps.2007.02.006
53. Gurtin, M.E., Anand, L.: A gradient theory for single-crystal plasticity. Model. Simul. Mater. Sci. **15**, S263–S270 (2007). doi:10.1088/0965-0393/15/1/S20
54. Gurtin, M.E.: The Burgers vector and the flow of screw and edge dislocations in finite-deformation single-crystal plasticity. J. Mech. Phys. Solids **54**, 1882–1898 (2006). doi:10.1016/j.jmps.2006.03.003
55. Gurtin, M.E., Anand, L.: A theory of strain-gradient plasticity for isotropic, plastically irrotational materials. Part I: small deformations. J. Mech. Phys. Solids **53**, 1624–1649 (2005b). doi:10.1016/j.jmps.2004.12.008
56. Gurtin, M.E., Anand, L.: A theory of strain-gradient plasticity for isotropic, plastically irrotational materials. Part II: finite deformations. Int. J. Plast. **21**, 2297–2318 (2005). doi:10.1016/j.ijplas.2005.01.006
57. Gurtin, M.E.: On a framework for small-deformation viscoplasticity: free energy, microforces, strain gradients. Int. J. Plast. **19**, 47–90 (2003). doi:10.1016/S0749-6419(01)00018-3
58. Bardella, L., Giacomini, A.: Influence of material parameters and crystallography on the size effects describable by means of strain gradient plasticity. J. Mech. Phys. Solids **56**, 2906–2934 (2008). doi:10.1016/j.jmps.2008.04.001
59. Bardella, L.: A deformation theory of strain gradient crystal plasticity that accounts for geometrically necessary dislocations. J. Mech. Phys. Solids **54**, 128–160 (2006). doi:10.1016/j.jmps.2005.08.003

60. Reddy, B.D.: The role of dissipation and defect energy in variational formulations of problems in strain-gradient plasticity. Part 2: single-crystal plasticity. Contin. Mech. T.hermodyn **23**, 551 (2011). doi:10.1007/s00161-011-0195-8
61. Reddy, B.D.: The role of dissipation and defect energy in variational formulations of problems in strain-gradient plasticity. Part 1: polycrystalline plasticity. Contin. Mech. Thermodyn. **23**, 527–549 (2011). doi:10.1007/s00161-011-0194-9
62. Arsenlis, A., Parks, D.M.: Crystallographic aspects of geometrically-necessary and statistically-stored dislocation density. Acta Mater. **47**, 1597–1611 (1999). doi:10.1016/S1359-6454(99)00020-8
63. Hirth, J.P., Lothe, J.: Theory of Dislocations. Wiley, New York (1982)
64. Teodosiu, C.: Elastic Models of Crystal Defects. Springer, Berlin (1982)
65. Voyiadjis, G.Z., Faghihi, D.: Thermo-mechanical strain gradient plasticity with energetic and dissipative length scales. Int. J. Plast. **30–31**, 218–247 (2012). doi:10.1016/j.ijplas.2011.10.007
66. Voyiadjis, G.Z., Al-Rub, R.K.A.: Gradient plasticity theory with a variable length scale parameter. Int. J. Solids Struct. **42**, 3998–4029 (2005). doi:10.1016/j.ijsolstr.2004.12.010
67. Clayton, J.D., McDowell, D.L., Bammann, D.J.: Modeling dislocations and disclinations with finite micropolar elastoplasticity. Int. J. Plast. **22**, 210–256 (2006). doi:10.1016/j.ijplas.2004.12.001
68. Levkovitch, V., Svendsen, B.: On the large-deformation- and continuum-based formulation of models for extended crystal plasticity. Int. J. Solids Struct. **43**, 7246–7267 (2006). doi:10.1016/j.ijsolstr.2006.05.010
69. Kuroda, M., Tvergaard, V.: A finite deformation theory of higher-order gradient crystal plasticity. J. Mech. Phys. Solids **56**, 2573–2584 (2008). doi:10.1016/j.jmps.2008.03.010
70. Kuroda, M.: On large-strain finite element solutions of higher-order gradient crystal plasticity. Int. J. Solids Struct. **48**, 3382–3394 (2011). doi:10.1016/j.ijsolstr.2011.08.008
71. Ertürk, İ., van Dommelen, J.A.W., Geers, M.G.D.: Energetic dislocation interactions and thermodynamical aspects of strain gradient crystal plasticity theories. J. Mech. Phys. Solids **57**, 1801–1814 (2009). doi:10.1016/j.jmps.2009.08.003
72. Svendsen, B., Bargmann, S.: On the continuum thermodynamic rate variational formulation of models for extended crystal plasticity at large deformation. J. Mech. Phys. Solids **58**, 1253–1271 (2010). doi:10.1016/j.jmps.2010.06.005
73. Ohno, N., Okumura, D.: Higher-order stress and grain size effects due to self-energy of geometrically necessary dislocations. J. Mech. Phys. Solids **55**, 1879–1898 (2007). doi:10.1016/j.jmps.2007.02.007
74. Ekh, M., Grymer, M., Runesson, K., Svedberg, T.: Gradient crystal plasticity as part of the computational modelling of polycrystals. Int. J. Numer. Methods Eng. **72**, 197–220 (2007). doi:10.1002/nme.2015
75. Bargmann, S., Svendsen, B., Ekh, M.: An extended crystal plasticity model for latent hardening in polycrystals. Comput. Mech. **48**, 631–645 (2011). doi:10.1007/s00466-011-0609-2
76. Klusemann, B., Svendsen, B., Bargmann, S.: Analysis and comparison of two finite element algorithms for dislocation density based crystal plasticity. GAMM Mitteilungen **36**, 219–238 (2013). doi:10.1002/gamm.201310013
77. Wulfinghoff, S., Böhlke, T.: Gradient crystal plasticity including dislocation-based work-hardening and dislocation transport. Int. J. Plast. **69**, 152–169 (2015). doi:10.1016/j.ijplas.2014.12.003
78. Evers, L.P., Brekelmans, W.A.M., Geers, M.G.D.: Non-local crystal plasticity model with intrinsic SSD and GND effects. J. Mech. Phys. Solids **52**, 2379–2401 (2004). doi:10.1016/j.jmps.2004.03.007
79. El-Naaman, S.A., Nielsen, K.L., Niordson, C.F.: On modeling micro-structural evolution using a higher order strain gradient continuum theory. Int. J. Plast. **76**, 285–298 (2016). doi:10.1016/j.ijplas.2015.08.008
80. Bargmann, S., Reddy, B.D.: Modeling of polycrystals using a gradient crystal plasticity theory that includes dissipative micro-stresses. Eur. J. Mech. A Solids **30**, 719–730 (2011). doi:10.1016/j.euromechsol.2011.04.006
81. Bargmann, S., Reddy, B.D., Klusemann, B.: A computational study of a model of single-crystal strain-gradient viscoplasticity with an interactive hardening relation. Int. J. Solids Struct. **51**, 2754–2764 (2014). doi:10.1016/j.ijsolstr.2014.03.010
82. Gurtin, M.E., Reddy, B.D.: Gradient single-crystal plasticity within a Mises–Hill framework based on a new formulation of self- and latent-hardening. J. Mech. Phys. Solids **68**, 134–160 (2014). doi:10.1016/j.jmps.2014.01.002
83. Gurtin, M.E., Ohno, N.: A gradient theory of small-deformation, single-crystal plasticity that accounts for GND-induced interactions between slip systems. J. Mech. Phys. Solids **59**, 320–343 (2011). doi:10.1016/j.jmps.2010.10.005
84. Gurtin, M.E., Reddy, B.D.: Some issues associated with the intermediate space in single-crystal plasticity. J. Mech. Phys. Solids **95**, 230–238 (2016). doi:10.1016/j.jmps.2016.05.027
85. Bonet, J., Wood, R.D.: Nonlinear Continuum Mechanics for Finite Element Analysis. Cambridge University Press, Cambridge (2008)
86. Bayerschen, E., Böhlke, T.: Power-law defect energy in a single-crystal gradient plasticity framework: a computational study. Comput. Mech. **58**, 13–27 (2016). doi:10.1007/s00466-016-1279-x
87. Wulfinghoff, S., Forest, S., Böhlke, T.: Strain gradient plasticity modeling of the cyclic behavior of laminate microstructures. J. Mech. Phys. Solids **79**, 1–20 (2015). doi:10.1016/j.jmps.2015.02.008
88. Forest, S., Guéninchault, N.: Inspection of free energy functions in gradient crystal plasticity. Acta Mech. Sin. **29**, 763–772 (2013). doi:10.1007/s10409-013-0088-0
89. Ohno, N., Okumura, D., Shibata, T.: Grain-size dependent yield behavior under loading, unloading and reverse loading. Int. J. Mod. Phys. B **22**, 5937–5942 (2008)
90. Bardella, L., Panteghini, A.: Modelling the torsion of thin metal wires by distortion gradient plasticity. J. Mech. Phys. Solids **78**, 467–492 (2015). doi:10.1016/j.jmps.2015.03.003
91. Anand, L., Gurtin, M.E., Reddy, B.D.: The stored energy of cold work, thermal annealing, and other thermodynamic issues in single crystal plasticity at small length scales. Int. J. Plast. **64**, 1–25 (2015). doi:10.1016/j.ijplas.2014.07.009
92. Pouriayevali, H., Xu, B.-X.: Decomposition of dislocation densities at grain boundary in a finite-deformation gradient crystal-plasticity framework. Int. J. Plast. (2017). doi:10.1016/j.ijplas.2017.04.010
93. Holzapfel, G.A.: Nonlinear Solid Mechanics: A Continuum Approach for Engineering. Wiley, Chichester (2000)
94. Zienkiewicz, O.C., Taylor, R.L.: The Finite Element Method for Solid and Structural Mechanics. Elsevier, Amsterdam (2005)
95. Huang, R., Li, Q.J., Wang, Z.J., Huang, L., Li, J., Ma, E., Shan, Z.W.: Flow stress in submicron BCC iron single crystals: sample-size-dependent strain-rate sensitivity and rate-dependent size strengthening. Mater. Res. Lett. **3**, 121–127 (2015). doi:10.1080/21663831.2014.999953